

# Estimating the seepage effect of SC-CO<sub>2</sub> and water fracturing with a steady-state flow model considering capillary and viscous forces at the pore scale

著者	Bailong Liu, Anna Suzuki, Takatoshi Ito
journal or publication title	Journal of Petroleum Science and Engineering
volume	184
page range	106483
year	2020-01
URL	<a href="http://hdl.handle.net/10097/00133823">http://hdl.handle.net/10097/00133823</a>

doi: 10.1016/j.petrol.2019.106483

Manuscript Number: PETROL15106R1

Title: Estimating the Seepage Effect of SC-CO<sub>2</sub> and Water Fracturing with a Steady-state Flow Model: Consider Capillary and Viscous Forces in Pore Scale

Article Type: Full Length Article

Keywords: Seepage effect; SC-CO<sub>2</sub> fracturing; Shale rock; Pore scale network model

Abstract: Supercritical carbon dioxide (SC-CO<sub>2</sub>) fracturing is a promising technology for unconventional energy development and carbon capture and storage. Experimental studies have shown that SC-CO<sub>2</sub> fracturing can form complex fracture networks and reduce crack initiation pressure, which are different results from those when fracturing with aqueous fluids. The complex fracture networks that form from SC-CO<sub>2</sub> fracturing may be the result of the strong seepage effect (i.e., low capillary and viscous forces). To understand the different injection behaviors induced by SC-CO<sub>2</sub> and aqueous fluids in low-permeability rocks, this study develops a new two-phase steady-state model based on the pore-scale network method. Although other models consider the viscous force, our model implements the capillary and viscous forces to reproduce the seepage effect. Because of the capillary force, the flow model is nonlinear and solved by iteratively solving matrix equations until a conservation of volumetric flux is satisfied. Simulation results show that the capillary force in a two-phase flow is not negligible on pressure distribution in small pore spaces. This leads to discontinuous pressure drops. This study shows that the seepage effect of SC-CO<sub>2</sub> is stronger than that of aqueous fluids.

Research Data Related to this Submission

-----  
Title: Data for: Estimating the Seepage Effect of SC-CO<sub>2</sub> and Water Fracturing with a Steady-state Flow Model: Consider Capillary and Viscous Forces in Pore Scale

Repository: Mendeley Data

<https://data.mendeley.com/datasets/78c992dpc8/draft?a=0c92bafb-a32c-4630-90e9-c5d3d3b2652f>

## Abstract

Supercritical carbon dioxide (SC-CO<sub>2</sub>) fracturing is a promising technology for unconventional energy development and carbon capture and storage. Experimental studies have shown that SC-CO<sub>2</sub> fracturing can form complex fracture networks and reduce crack initiation pressure, which are different results from those when fracturing with aqueous fluids. The complex fracture networks that form from SC-CO<sub>2</sub> fracturing may be the result of the strong seepage effect (i.e., low capillary and viscous forces). To understand the different injection behaviors induced by SC-CO<sub>2</sub> and aqueous fluids in low-permeability rocks, this study develops a new two-phase steady-state model based on the pore-scale network method. Although other models consider the viscous force, our model implements the capillary and viscous forces to reproduce the seepage effect. Because of the capillary force, the flow model is nonlinear and solved by iteratively solving matrix equations until a conservation of volumetric flux is satisfied. Simulation results show that the capillary force in a two-phase flow is not negligible on pressure distribution in small pore spaces. This leads to discontinuous pressure drops. This study shows that the seepage effect of SC-CO<sub>2</sub> is stronger than that of aqueous fluids.

**Keyword: Seepage effect; SC-CO<sub>2</sub> fracturing; Shale rock; Pore scale network model**

1 We have read the comments of reviewers and editors. These comments have been  
2 constructively helpful to our article. In order to answer the comments of the reviewers,  
3 we divided the opinions into five major questions as follows:

4 **Reviewers 1:**

5 **1. The fact that this model assumes steady-state conditions should be mentioned**  
6 **much earlier (including possibly the title) and more often.**  
7

8  
9 We modified the title, body, conclusion of this papers as your suggested.

10  
11 **2. Therefore, there may very well be capillary resistance during at least some (if**  
12 **not all) of the period of most interest (i.e., injection). This should at least be**  
13 **discussed and considered in the manuscript.**  
14  
15

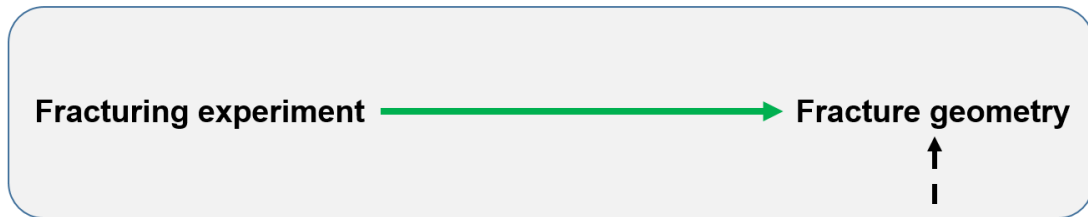
16  
17 According reviewer's comment, we added contents to discuss this problem.  
18 Fracturing process contains a pressurization stage by injecting fracturing fluid into a  
19 borehole. If this period is long enough, the fracturing fluid is mixed well with the  
20 formation fluid (e.g., hydrocarbon) and the capillary resistance can be neglected. In  
21 the experiment from Zhang et al. (2017), the period of SC-CO<sub>2</sub> injection was over 7.0  
22 minutes. We expect that this period could be long enough to mix between SC-CO<sub>2</sub>  
23 and formation fluid in the view of the high diffusion coefficient of SC-CO<sub>2</sub>. Even if  
24 the pressurization stage is not enough to make two different fluid mix well, the  
25 interfacial tension between SC-CO<sub>2</sub> and hydrocarbon is ultra-small. The interfacial  
26 tension between SC-CO<sub>2</sub> and hydrocarbon (gas) is less than 2mN/m (Li et al., 2017),  
27 while the interfacial tension between water and hydrocarbon (gas) is about 50mN/m.  
28 The capillary force between SC-CO<sub>2</sub> and hydrocarbon is much smaller than that  
29 between water and hydrocarbon. Thus, the effect of capillary force that occurs with  
30 SC-CO<sub>2</sub> is quite smaller than with water. Therefore, the capillary force between  
31 SC-CO<sub>2</sub> and formation fluid is neglected in our simulation.  
32  
33

34  
35 **3. While the authors drew good comparisons between their modeling outputs and**  
36 **analytical solutions, I wonder why more effort was not given to match their**  
37 **models with the experimental results they reference so often (Zhang et al., 2017).**  
38 **There may be a very plausible explanation for this. If so, it should be mentioned.**  
39 **If not, I believe a comparison to these data is warranted.**  
40  
41

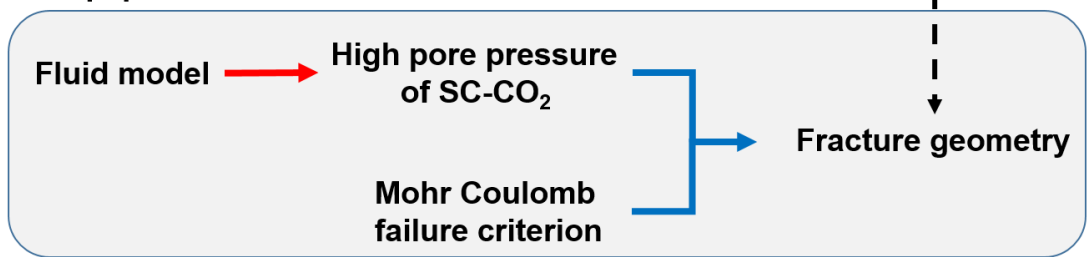
42  
43 Their experiment (Zhang et al., 2017) were conducted to study different fracture  
44 patterns induced by water injection and SC-CO<sub>2</sub> injection. They indicated that the  
45 mechanism of forming complex fracture patterns was the effect of strong seepage  
46 effect. Thus, understanding of flow behaviors of SC-CO<sub>2</sub> is a challenge that must be  
47 overcome in the beginning, and is essential for reproducing complex fracture patterns.  
48 Therefore, this paper focuses on developing a new flow model considering the effects  
49 of viscous and capillary forces. Our results indicated that SC-CO<sub>2</sub> injection leads to  
50 relatively high pore pressure distributions in a wide area away from the well. Based  
51 on the Mohr-Coulomb failure criterion, the high pore pressure distributions likely  
52 results in shear failure in a wide area and should generate complex fracture  
53  
54  
55  
56  
57  
58  
59  
60  
61  
62  
63  
64  
65

distributions. This finding is consistent with the experimental results. If the experiment could provide pore pressure distributions, we could compare pressure distributions with our simulation results. However, it is difficult to measure pore pressure distributions in an experiment, and their paper presented fracture geometries only. Thus, in this paper comparison with experimental results was in discussion only. We argued this in our manuscript. In our future work, we will develop a solid model and couple it with the current flow model to simulate fracture geometry and compare with the experiment result (Zhang et al., 2017) directly.

**Zhang's experiment:**

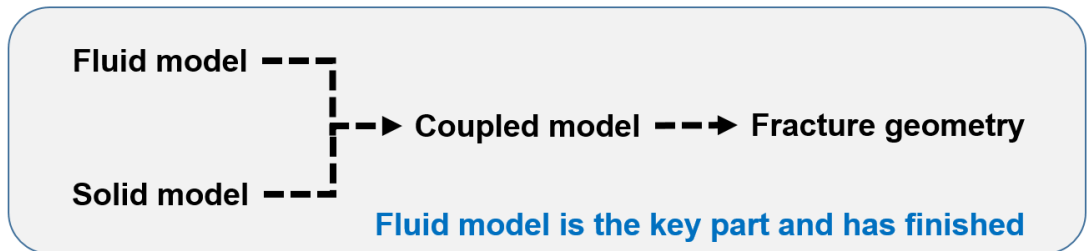


**Our paper:**



→ Numerical simulation      → Inference

**Future work:**



**4. Lastly, the writing of this manuscript needs a lot of work before it is publishable.**

Thanks for suggestion about the writing. We amended the figures and sentences. In addition, the article was checked by native speaker.

**Reviewers 2:**

**5. The abstract and Fig problems**

According to the comment of reviewer, we delete the Fig.1 and add more details of the flow model in the abstract.

1           **Reference**

2           Li, N., Zhang, C.W., Ma, Q.L., Jiang, L.Y., Xu, Y.X., Chen, G.J., Sun, C.Y., Yang,  
3           L.Y., 2017. Interfacial Tension Measurement and Calculation of (Carbon Dioxide  
4           + n-Alkane) Binary Mixtures. *J. Chem. Eng. Data* 62, 2861–2871.  
5           <https://doi.org/10.1021/acs.jced.7b00159>  
6

7  
8  
9  
10          Zhang, X., Lu, Y., Tang, J., Zhou, Z., Liao, Y., 2017. Experimental study on fracture  
11          initiation and propagation in shale using supercritical carbon dioxide fracturing.  
12          *Fuel* 190, 370–378. <https://doi.org/10.1016/j.fuel.2016.10.120>  
13  
14  
15  
16  
17  
18  
19  
20  
21  
22  
23  
24  
25  
26  
27  
28  
29  
30  
31  
32  
33  
34  
35  
36  
37  
38  
39  
40  
41  
42  
43  
44  
45  
46  
47  
48  
49  
50  
51  
52  
53  
54  
55  
56  
57  
58  
59  
60  
61  
62  
63  
64  
65

# Estimating the Seepage Effect of SC-CO<sub>2</sub> and Water Fracturing with a Steady-state Flow Model: Consider Capillary and Viscous Forces in Pore Scale

Bailong Liu, Anna Suzuki, and Takatoshi Ito

Institute of Fluid Science, Tohoku University., Japan

## Abstract

Supercritical carbon dioxide (SC-CO<sub>2</sub>) fracturing is a promising technology for unconventional energy development and carbon capture and storage. Experimental studies have shown that SC-CO<sub>2</sub> fracturing can form complex fracture networks and reduce crack initiation pressure, which are different results from those when fracturing with aqueous fluids. The complex fracture networks that form from SC-CO<sub>2</sub> fracturing may be the result of the strong seepage effect (i.e., low capillary and viscous forces). To understand the different injection behaviors induced by SC-CO<sub>2</sub> and aqueous fluids in low-permeability rocks, this study develops a new two-phase steady-state model based on the pore-scale network method. Although other models consider the viscous force, our model implements the viscous and capillary forces to reproduce the seepage effect. Because of the capillary force, the flow model is nonlinear and solved by iteratively solving matrix equations until a conservation of volumetric flux is satisfied. Simulation results show that the capillary force in a two-phase flow is not negligible on pressure distribution in small pore spaces. This leads to discontinuous pressure drops. This study shows that the seepage effect of SC-CO<sub>2</sub> is stronger than that of aqueous fluids.

**Keyword:** Seepage effect; SC-CO<sub>2</sub> fracturing; Shale rock; Pore scale network

1 **model**

2  
3 **1. Introduction**

4  
5  
6 Supercritical carbon dioxide (SC-CO<sub>2</sub>) is a special fluid with a low viscosity  
7  
8 (like gas) and high density (like liquid). Experimental studies have shown that  
9  
10 SC-CO<sub>2</sub> has many potential advantages as a fracturing fluid. For instance, SC-CO<sub>2</sub>  
11  
12 fracturing reduces initiation pressure by 50% or more (Zhang et al., 2017). Fractures  
13  
14 induced by SC-CO<sub>2</sub> are irregular multiple cracks and easily form complex fracture  
15  
16 networks, which are different from fractures induced by conventional aqueous fluids  
17  
18 (Bennour et al., 2015; Ishida et al., 2016a; Zhang et al., 2017). These characteristics  
19  
20 of SC-CO<sub>2</sub> fracturing yield positive effects on unconventional energy developments,  
21  
22 including CO<sub>2</sub> sequestration and enhanced geothermal systems (Middleton et al., 2014;  
23  
24 Reynolds et al., 2018).

25  
26  
27  
28  
29  
30  
31  
32  
33  
34 Injected water can be an immiscible fluid in oil and gas reservoirs, whereas  
35  
36 injected SC-CO<sub>2</sub> can be a miscible fluid. When comparing water injection and  
37  
38 SC-CO<sub>2</sub> injection, two-phase flow should be considered. In addition, the different  
39  
40 performances of SC-CO<sub>2</sub> fracturing from aqueous fluid fracturing are generally  
41  
42 considered to derive from the strong seepage effects of SC-CO<sub>2</sub> (Ishida et al., 2016;  
43  
44 Watanabe et al., 2017; Zhang et al., 2017). The seepage effect may be influenced by  
45  
46 capillary and viscous forces in small pore spaces in a two-phase flow (Kantzas,  
47  
48 Apostolos; Bryan Jonathan; Taheri, 2015). Strong seepage effects occur because of  
49  
50 low viscous and low capillary forces, which may lead to increased percolation and  
51  
52 increased pore pressure. Some studies have investigated pore pressure distribution  
53  
54  
55  
56  
57  
58  
59  
60  
61  
62  
63  
64  
65



1 during fracturing, but their flow models have considered only the viscous force  
2  
3 (Belytschko et al., 2000; Choo et al., 2016; Economides and Boney, 2000; Latham et  
4  
5 al., 2011; Lecampion et al., 2017; Liu et al., 2018; Peng et al., 2017; Shi et al., 2017;  
6  
7 Shimizu et al., 2011; Yan et al., 2016; Zhao et al., 2014). The capillary force cannot be  
8  
9 ignored in low-permeability porous media such as shale rock when a two-phase flow  
10  
11 occurs (Blunt, 2001; Higdon, 2013).  
12  
13  
14  
15  
16

17 The pore-scale network model (PNM) has been developed to simulate flow in  
18  
19 porous media (Valvatne, 2004), and some studies have simulated the multiphase flow  
20  
21 in the pore scale using a PNM (Al-Gharbi and Blunt, 2005; Joekar-Niasar and  
22  
23 Hassanizadeh, 2012; Wang et al., 2015). Because a PNM can consider small pore  
24  
25 geometries, it is used to closely examine behaviors in the pore space.  
26  
27  
28  
29  
30

31 In this study, a two-phase steady-state flow model is developed to investigate the  
32  
33 seepage effects of SC-CO<sub>2</sub>. The model integrates both capillary and viscous forces  
34  
35 based on the PNM. We analyze the characteristics of the pressure field during fluid  
36  
37 injection, which directly influence fracture geometries during fracturing. In addition,  
38  
39 the difference between injection SC-CO<sub>2</sub> and injection water is discussed.  
40  
41  
42  
43  
44

## 45 2. Model description

### 46 2.1 Pore-scale network models

47  
48 The PNM is an effective model to represent flow in a porous medium through the  
49  
50 pores and throats. In the fracturing process, injection fluid is pushed into formations,  
51  
52 and the formation fluid is displaced. In general, three types of displacements can  
53  
54 occur during fracturing: piston-like, pore-body filling, or snap-off (Valvatne, 2004).  
55  
56  
57  
58  
59  
60  
61  
62  
63  
64  
65

1 The piston-like displacement refers to invasion into throats by fluid that were  
2 previously present in pores. In a pore-body filling displacement, fluid in pores is  
3 displaced by the fluid in throats. Snap-off displacement describes invasion by wetting  
4 fluid at the corner of a cross section when the pressure of the invasion fluid is lower  
5 than the threshold of the capillary pressure. The effect of snap-off displacement is  
6 known to be considerably smaller than the effects of the other two types of  
7 displacements in shale rocks (Al-Gharbi and Blunt, 2005). Thus, the current model  
8 considers only piston-like displacement and pore-body filling. In our network model,  
9 the triangular cross section was selected to consider the wetting phase flow (film flow)  
10 at the corners (Mogensen and Stenby, 1998; Nguyen et al., 2006).

27 Let us consider that there are two adjacent elements  $i$  and  $j$ . (Note that whether  
28 they are pores or throats is irrelevant.) The flow rate from element  $i$  to element  $j$ ,  
29  $q_{ij}$ , is given by:

$$q_{ij} = g_{ij}(P_i - P_j + P_{c,ij}) \quad \#(1)$$

36 where  $g_{ij}$  is the flow conductivity between elements  $i$  and  $j$ .  $P_i$  and  $P_j$  are the  
37 pressures for elements  $i$  and  $j$ , respectively.  $P_{c,ij}$  is the capillary force between  
38 elements  $i$  and  $j$ . The flow conductivity equations are given by (Hughes and Blunt,  
39 2000):

$$g_{ij} = \int_0^L g(x) dx \quad \#(2)$$

$$g(x) = 1/C(x), 0 \leq x \leq L \quad \#(3)$$

47 where  $\mu$  is the fluid viscosity,  $L$  is the length between elements  $i$  and  $j$ , and  $C(x)$   
48 is the fluid conductance per unit length and is determined by the fluid configuration in

1 their cross sections.

2  
3 Two types of cross-section configurations (see Fig. 1(a)) can be generated when  
4 the injection fluid is different from the formation fluid: single-phase configuration (in  
5 a non-invaded element),  $C_{sp}$ ; and two-phase configuration (in an invaded element),  
6  $C_{tp}$ . The geometric parameters for calculating conductance and area are shown in Fig.  
7  
8  
9  
10  
11  
12  
13  
14  
15  
16  
17  
18  
19  
20  
21  
22  
23  
24  
25  
26  
27  
28  
29  
30  
31  
32  
33  
34  
35  
36  
37  
38  
39  
40  
41  
42  
43  
44  
45  
46  
47  
48  
49  
50  
51  
52  
53  
54  
55  
56  
57  
58  
59  
60  
61  
62  
63  
64  
65

For single-phase configuration, the fluid conductance per unit length,  $C_{sp}$ , is given by (Aker et al., 1998; Al-Gharbi, 2004):

$$C_{sp} = \frac{\pi\mu_w}{128} \left( R + (A_t/\pi)^{\frac{1}{2}} \right)^4 \quad \#(4)$$

where  $A_t$  is the cross-section area of the element and  $R$  is the inscribed radius of the cross section. The cross-section area of the element,  $A_t$ , is:

$$A_t = R^2 \sum_{i=1}^n \cot \alpha_i \quad \#(5)$$

where  $\alpha_i$  is the half corner angle and  $n$  is the number of corners in the cross section.

For two-phase configuration, the wetting and non-wetting phases in the cross section should be considered. The fluid conductance per unit length for the two-phase configuration,  $C_{tp}$ , is described by:

$$C_{tp} = (C_{nw} + C_w) / C_{nw} C_w \quad \#(6)$$

where  $C_{nw}$  and  $C_w$  represent the conductance of the non-wetting phase and wetting phase fluids in the center and at the corner, respectively, which is given by (Aker et al., 1998; Al-Gharbi, 2004):

$$C_{nw} = \frac{\pi\mu_{nw}}{128} \left( R + (A_{nw}/\pi)^{\frac{1}{2}} \right)^4 \quad \#(7)$$

$$C_w = \mu_w \sum_{i=1}^n \left( \frac{A_{ci}(1 - \sin \alpha_i)\varphi_3}{\sin \alpha_i (1 - \varphi_3)(\varphi_2 + f\varphi_1)} \cdot \left( \frac{\varphi_2 \cos \theta - \varphi_1}{12} \right)^{\frac{1}{2}} \right)^2 \#(8)$$

The parameters  $\varphi_1$ ,  $\varphi_2$ , and  $\varphi_3$  depend on the half corner angle  $\alpha$  and the contact angle  $\theta$ . The parameter  $f$  indicates the capacity of fluid crossing the fluid interface (Piri and Blunt, 2005). In our model, the parameter  $f$  equals 1, which means that no flow occurs on the fluid interface. The area of the formation fluid (wetting phase fluid) at the corner,  $A_w$ , and injection fluid (non-wetting phase fluid) at the center,  $A_{nw}$ , are calculated by:

$$A_w = \sum_{i=1}^n A_{ci} \#(9)$$

$$A_{ci} = r^2 \left( \cos \theta (\cot \alpha_i \cos \theta - \sin \theta) + \theta + \alpha_i - \frac{\pi}{2} \right) \#(10)$$

$$A_{nw} = A_t - A_w \#(11)$$

where  $r$  is the radius of the curvature of the interface.

For elements invaded by injection fluid (see Fig. 1(b)), the flow rate  $q_{ij}$  as given in the following equation is divided into the flow rates of the wetting and non-wetting phases as:

$$q_{ij} = q_{nw,ij} + q_{w,ij} \#(12)$$

The flow rate of each phase from element  $i$  to element  $j$  is given by:

$$q_{nw,ij} = q_{ij} C_{nw,i} / (C_{nw,i} + C_{w,i}) \#(13)$$

$$q_{w,ij} = q_{ij} C_{w,i} / (C_{nw,i} + C_{w,i}) \#(14)$$

where  $C_{w,i}$  and  $C_{nw,i}$  represent the conductance of the non-wetting and wetting phase fluids in element  $i$ , respectively.

The capillary force ( $P_{c,ij}$ ) between element  $i$  and  $j$  is calculated using the

1 Young–Laplace equation:

$$2 P_{c,ij} = \frac{2\sigma \cos \theta}{r} \#(15)$$

3 where  $\sigma$  denotes interfacial tension between the two fluid phases.

4  
5  
6  
7  
8  
9 Considering the small compressibility of SC-CO<sub>2</sub> (Vilarrasa et al., 2010), the  
10 conservation equation is applicable to SC-CO<sub>2</sub> flow. For either single- or two-phase  
11 flow, the conservation of the volume flux at element  $i$  can be described by:

$$12 \sum_{j=1}^{Z_i} q_{ij} = \sum_{j=1}^{Z_i} (q_{nw,ij} + q_{w,ij}) = 0 \#(16)$$

13  
14  
15  
16  
17  
18  
19  
20  
21 where  $Z_i$  is the number of elements connecting to element  $i$ . For instance, the pore  $i$   
22 connects throats 1–3 in Fig. 2. The conservation of volume flux at pore  $i$  can be  
23 expressed as  $q_{i2} + q_{i3} + q_{i1} = 0$ .

24  
25  
26  
27  
28  
29  
30 Each pore connects more than one throat in our numerical model. Based on the  
31 flow rate of (1) – (16) and the topological structure of the network, the assembly  
32 equation can be formed as:

$$33 \begin{bmatrix} D_{11} & \cdots & D_{1j} \\ \vdots & \ddots & \vdots \\ D_{i1} & \cdots & D_{ij} \end{bmatrix} \begin{Bmatrix} P_1 \\ \vdots \\ P_i \end{Bmatrix} = \begin{Bmatrix} \sum_{j=1}^{Z_1} g_{1j} P_{c,1j} \\ \vdots \\ \sum_{j=1}^{Z_i} g_{ij} P_{c,ij} \end{Bmatrix} \#(17)$$

34  
35  
36  
37  
38  
39  
40  
41  
42  
43  
44  
45  
46  
47  
48  
49  
50  
51  
52  
53  
54  
55  
56  
57  
58  
59  
60  
61  
62  
63  
64  
65  
66  
67  
68  
69  
70  
71  
72  
73  
74  
75  
76  
77  
78  
79  
80  
81  
82  
83  
84  
85  
86  
87  
88  
89  
90  
91  
92  
93  
94  
95  
96  
97  
98  
99  
100  
101  
102  
103  
104  
105  
106  
107  
108  
109  
110  
111  
112  
113  
114  
115  
116  
117  
118  
119  
120  
121  
122  
123  
124  
125  
126  
127  
128  
129  
130  
131  
132  
133  
134  
135  
136  
137  
138  
139  
140  
141  
142  
143  
144  
145  
146  
147  
148  
149  
150  
151  
152  
153  
154  
155  
156  
157  
158  
159  
160  
161  
162  
163  
164  
165  
166  
167  
168  
169  
170  
171  
172  
173  
174  
175  
176  
177  
178  
179  
180  
181  
182  
183  
184  
185  
186  
187  
188  
189  
190  
191  
192  
193  
194  
195  
196  
197  
198  
199  
200  
201  
202  
203  
204  
205  
206  
207  
208  
209  
210  
211  
212  
213  
214  
215  
216  
217  
218  
219  
220  
221  
222  
223  
224  
225  
226  
227  
228  
229  
230  
231  
232  
233  
234  
235  
236  
237  
238  
239  
240  
241  
242  
243  
244  
245  
246  
247  
248  
249  
250  
251  
252  
253  
254  
255  
256  
257  
258  
259  
260  
261  
262  
263  
264  
265  
266  
267  
268  
269  
270  
271  
272  
273  
274  
275  
276  
277  
278  
279  
280  
281  
282  
283  
284  
285  
286  
287  
288  
289  
290  
291  
292  
293  
294  
295  
296  
297  
298  
299  
300  
301  
302  
303  
304  
305  
306  
307  
308  
309  
310  
311  
312  
313  
314  
315  
316  
317  
318  
319  
320  
321  
322  
323  
324  
325  
326  
327  
328  
329  
330  
331  
332  
333  
334  
335  
336  
337  
338  
339  
340  
341  
342  
343  
344  
345  
346  
347  
348  
349  
350  
351  
352  
353  
354  
355  
356  
357  
358  
359  
360  
361  
362  
363  
364  
365  
366  
367  
368  
369  
370  
371  
372  
373  
374  
375  
376  
377  
378  
379  
380  
381  
382  
383  
384  
385  
386  
387  
388  
389  
390  
391  
392  
393  
394  
395  
396  
397  
398  
399  
400  
401  
402  
403  
404  
405  
406  
407  
408  
409  
410  
411  
412  
413  
414  
415  
416  
417  
418  
419  
420  
421  
422  
423  
424  
425  
426  
427  
428  
429  
430  
431  
432  
433  
434  
435  
436  
437  
438  
439  
440  
441  
442  
443  
444  
445  
446  
447  
448  
449  
450  
451  
452  
453  
454  
455  
456  
457  
458  
459  
460  
461  
462  
463  
464  
465  
466  
467  
468  
469  
470  
471  
472  
473  
474  
475  
476  
477  
478  
479  
480  
481  
482  
483  
484  
485  
486  
487  
488  
489  
490  
491  
492  
493  
494  
495  
496  
497  
498  
499  
500  
501  
502  
503  
504  
505  
506  
507  
508  
509  
510  
511  
512  
513  
514  
515  
516  
517  
518  
519  
520  
521  
522  
523  
524  
525  
526  
527  
528  
529  
530  
531  
532  
533  
534  
535  
536  
537  
538  
539  
540  
541  
542  
543  
544  
545  
546  
547  
548  
549  
550  
551  
552  
553  
554  
555  
556  
557  
558  
559  
560  
561  
562  
563  
564  
565  
566  
567  
568  
569  
570  
571  
572  
573  
574  
575  
576  
577  
578  
579  
580  
581  
582  
583  
584  
585  
586  
587  
588  
589  
590  
591  
592  
593  
594  
595  
596  
597  
598  
599  
600  
601  
602  
603  
604  
605  
606  
607  
608  
609  
610  
611  
612  
613  
614  
615  
616  
617  
618  
619  
620  
621  
622  
623  
624  
625  
626  
627  
628  
629  
630  
631  
632  
633  
634  
635  
636  
637  
638  
639  
640  
641  
642  
643  
644  
645  
646  
647  
648  
649  
650  
651  
652  
653  
654  
655  
656  
657  
658  
659  
660  
661  
662  
663  
664  
665  
666  
667  
668  
669  
670  
671  
672  
673  
674  
675  
676  
677  
678  
679  
680  
681  
682  
683  
684  
685  
686  
687  
688  
689  
690  
691  
692  
693  
694  
695  
696  
697  
698  
699  
700  
701  
702  
703  
704  
705  
706  
707  
708  
709  
710  
711  
712  
713  
714  
715  
716  
717  
718  
719  
720  
721  
722  
723  
724  
725  
726  
727  
728  
729  
730  
731  
732  
733  
734  
735  
736  
737  
738  
739  
740  
741  
742  
743  
744  
745  
746  
747  
748  
749  
750  
751  
752  
753  
754  
755  
756  
757  
758  
759  
760  
761  
762  
763  
764  
765  
766  
767  
768  
769  
770  
771  
772  
773  
774  
775  
776  
777  
778  
779  
780  
781  
782  
783  
784  
785  
786  
787  
788  
789  
790  
791  
792  
793  
794  
795  
796  
797  
798  
799  
800  
801  
802  
803  
804  
805  
806  
807  
808  
809  
810  
811  
812  
813  
814  
815  
816  
817  
818  
819  
820  
821  
822  
823  
824  
825  
826  
827  
828  
829  
830  
831  
832  
833  
834  
835  
836  
837  
838  
839  
840  
841  
842  
843  
844  
845  
846  
847  
848  
849  
850  
851  
852  
853  
854  
855  
856  
857  
858  
859  
860  
861  
862  
863  
864  
865  
866  
867  
868  
869  
870  
871  
872  
873  
874  
875  
876  
877  
878  
879  
880  
881  
882  
883  
884  
885  
886  
887  
888  
889  
890  
891  
892  
893  
894  
895  
896  
897  
898  
899  
900  
901  
902  
903  
904  
905  
906  
907  
908  
909  
910  
911  
912  
913  
914  
915  
916  
917  
918  
919  
920  
921  
922  
923  
924  
925  
926  
927  
928  
929  
930  
931  
932  
933  
934  
935  
936  
937  
938  
939  
940  
941  
942  
943  
944  
945  
946  
947  
948  
949  
950  
951  
952  
953  
954  
955  
956  
957  
958  
959  
960  
961  
962  
963  
964  
965  
966  
967  
968  
969  
970  
971  
972  
973  
974  
975  
976  
977  
978  
979  
980  
981  
982  
983  
984  
985  
986  
987  
988  
989  
990  
991  
992  
993  
994  
995  
996  
997  
998  
999  
1000

where  $D_{ij}$  is the conductance matrix. When  $i = j$ ,  $D_{ij} = \sum_{j=1}^{Z_i} g_{ij}$ ; otherwise,  
 $D_{ij} = g_{ij}$ .

## 2.2 Computational procedure

Based on the previous discussion, we derived the quasi-steady-state pressure distribution. To simulate fluid injection, a time variation of the fluid flow was calculated. We iterated to obtain the steady-state pressure distribution at each time

step  $\Delta t$ . The computational procedure, as shown in Fig. 3, is described as follows:

1) Based on the initial condition, the conductivity of each element is calculated by using (4) – (11). Then, the integral conductance matrix  $D_{ij}$  and force matrix are assembled.

2) As  $P_{outlet}^t$  and  $P_{inlet}^t$  are known, the pressure distribution is obtained from (17). Based on the pressure distribution, the total flow rate  $q_{ij}$ , the non-wetting phase flow rate  $q_{nw,ij}$ , and the wetting phase flow rate  $q_{w,ij}$  can be solved through (1) and (12) – (14).

3) Calculate each phase fluid volume  $V_{w,i}^{t+\Delta t}$  and  $V_{nw,i}^{t+\Delta t}$  in element  $i$  at  $t + \Delta t$  by using (18) – (19). Update the meniscus position and fluid configuration of each element based on each phase fluid volume. The purpose of choosing  $\Delta t$  is to ensure every meniscus will not cross one throat element in  $\Delta t$ . Then, the initial condition can be updated according to the configuration at  $t + \Delta t$ .

The volume of each of the wetting and non-wetting phases in element  $i$  can be expressed by:

$$V_{w,i}^{t+\Delta t} = V_{w,i}^t + \Delta t \times \sum_{j=1}^{Z_i} q_{w,ij} \quad \#(18)$$

$$V_{nw,i}^{t+\Delta t} = V_{nw,i}^t + \Delta t \times \sum_{j=1}^{Z_i} q_{nw,ij} \quad \#(19)$$

### 3. Simulation condition

We simulated seepage effects (capillary and viscous forces) for SC-CO<sub>2</sub> and water fracturing as previously examined in the SC-CO<sub>2</sub> and water fracturing experiment conducted by Zhang et al (Zhang et al., 2017).

### 3.1 Structure of PNM

Two pore network structures were used in the simulation cases. One structure, labeled Network A, was used to validate the flow model and investigate the difference between injecting SC-CO<sub>2</sub> and water, as shown in Fig. 4(a). Network A was used to represent two types of porous media: homogenous porous medium (PNM-homo) and heterogeneous porous medium (PNM-hetero). For PNM-homo, a constant average radius of pores and throats was set for a single simulation. To investigate the effects of different radii, the radii of pores and throats varied from 0.01 to 0.15  $\mu\text{m}$  for each simulation. Thus, the sizes of the simulation models varied for different average radii of pores and throats, see Table 1. The lengths were normalized by the size of each simulation model. For PNM-hetero, the distributions of radii of throats and pores were generated based on the statistical data of sandstone (Bakke and Øren, 1997; Øren and Bakke, 2003, 2002), which is shown in Fig. 5. The other structure, Network B, was assumed to contain a pre-existing fracture (PNM-frac), which was to see pressure distribution around fracture. (see Fig. 4(b)). The size of Network B was consistent with the experimental sample of Zhang et al. (Zhang et al., 2017).

### 3.2 Fluid parameter and injection pressure

Four fluid systems and fluid viscosities, as listed in Tables 2 and 3, respectively, were used in the simulation and considered in the discussion. The formation fluid was gas or oil and the injection fluid was oil, water, or SC-CO<sub>2</sub>. SC-CO<sub>2</sub> is miscible with hydrocarbons and has a high diffusion coefficient. In the fracturing process, a pressurization stage occurs before crack initiation. At this pressurization stage, SC-CO<sub>2</sub> can fully dissolve with the formation fluid at the interface area. The interface between SC-CO<sub>2</sub> and hydrocarbon (gas or oil) disappears and the capillary force

1 decreases to zero. Before SC-CO<sub>2</sub> dissolves sufficiently into a formation fluid, the  
2  
3 interfacial tension between SC-CO<sub>2</sub> and hydrocarbon is very small, approximately 2  
4  
5 mN/m (Li et al., 2017). The interfacial tension between water and hydrocarbon is  
6  
7 approximately 50 mN/m. Thus, our simulation assumed that the capillary force  
8  
9 between SC-CO<sub>2</sub> and the formation fluids (oil or gas) was negligible.  
10  
11  
12

13  
14 The inlet and outlet pressure values were derived from the fracturing  
15  
16 experimental conditions of Zhang et al. (Zhang et al., 2017). In their experiment, the  
17  
18 injection pressure was approximately 5 MPa after fracture initiation. Considering the  
19  
20 pressure loss in tube, 4 MPa was used as the inlet pressure. However, 8 MPa was also  
21  
22 set as the inlet pressure to ensure that the inlet pressure was higher than the threshold  
23  
24 of the capillary force for different radii.  
25  
26  
27  
28  
29  
30

#### 31 4. Validation

32  
33 A validation of the flow model was conducted by comparing the analytical  
34  
35 solutions in different flow situations: a) single-phase flow (the injection and formation  
36  
37 fluids were the same); b) two-phase flow without considering the capillary force ( $P_c$ ).  
38  
39  
40 The analytical solutions were based on the Buckley-Leverett theory (Buckley and  
41  
42 Leverett, 1942; Idowu and Blunt, 2010). These solutions and the numerical results  
43  
44 obtained from the flow model are plotted in Fig. 6. The numerical results of the  
45  
46 single- and two-phase flows without capillary force were confirmed to be in good  
47  
48 agreement with the analytical results derived from the homogeneous porous medium.  
49  
50  
51  
52  
53  
54

#### 55 5. Simulation and results

56  
57  
58 To investigate the seepage effects of SC-CO<sub>2</sub> injection, five simulations were  
59  
60  
61  
62  
63  
64  
65



1 conducted. Both capillary and viscous forces were integrated into the PNM to  
2  
3 simulate the pressure field for a two-phase flow. The different injection conditions are  
4  
5 listed in Table 4.  
6  
7

### 8 9 **5.1 Effects of capillary force**

10  
11 The effects of capillary force on two-phase flow are presented in Fig. 7. The  
12 PNM-homo was used to simulate the effect of the capillary force. The constant  
13 pore-throat radius was set to  $0.1 \mu m$ . The results yielded snapshots of the pressure  
14 distributions derived from water injection with and without capillary force. Water was  
15 injected from the inlet (normalized length = 0). The case without  $P_c$  only considered  
16 the effect of viscous force, whereas that with  $P_c$  considered the effects of both viscous  
17 and capillary forces. When the capillary force was considered, a discontinuous  
18 pressure drop (DPD) occurred. The capillary force posed an extra resistant force to  
19 block the invasion of water. This resistant force derived from the capillary force could  
20 cause a DPD in the two-phase flow.  
21  
22  
23  
24  
25  
26  
27  
28  
29  
30  
31  
32  
33  
34  
35  
36  
37

### 38 39 **5.2 Effects of injection time**

40  
41 Water or SC-CO<sub>2</sub> injections were simulated in a homogeneous porous medium  
42 using PNM-homo. The constant average pore-throat radius was  $0.1 \mu m$ . The time  
43 variation of the pressure field is shown in Fig. 8. Water or SC-CO<sub>2</sub> was injected from  
44 the inlet (normalized length = 0), and the pressure field of the water injection, as  
45 shown in Fig.8(a), experienced a DPD that was caused by the capillary force. The  
46 injection fluid (water) was immiscible with the formation fluid (oil). When they met  
47 during injection, the capillary force was generated at the interface between water and  
48  
49  
50  
51  
52  
53  
54  
55  
56  
57  
58  
59  
60  
61  
62  
63  
64  
65

1 oil. With continuous injection, DPD continuously affected the pressure field. The  
2 positions of the DPD moved to the outlet side because of changes in the  
3 interfacial  
4 position between water and oil.  
5  
6

7  
8 By contrast, the pressure field of the SC-CO<sub>2</sub> injection experienced no DPD, as  
9 shown in Fig. 8(b). Because SC-CO<sub>2</sub> and oil are miscible, no interface existed  
10 between them. In other words, no capillary force occurred between SC-CO<sub>2</sub> and oil,  
11 which means that no DPD occurred. Fig. 8(b) also shows that the slope of the pressure  
12 curve in the area displaced by SC-CO<sub>2</sub> (inlet side) was flatter than the area occupied  
13 by oil (outlet side). This was caused by both low viscous and low capillary forces of  
14 SC-CO<sub>2</sub>, (i.e., the seepage effect). Because the injected SC-CO<sub>2</sub> penetrated into pores  
15 easily given a small pressure drop, pressure propagation was advanced with a value  
16 that approximated the injection pressure. The change points of slopes could be  
17 considered the interfacial positions between SC-CO<sub>2</sub> and oil. The interfacial position  
18 between SC-CO<sub>2</sub> and oil was ahead of that between water and oil. This indicated that  
19 the seepage effect of SC-CO<sub>2</sub> promoted the advancement of the interfacial front.  
20  
21  
22  
23  
24  
25  
26  
27  
28  
29  
30  
31  
32  
33  
34  
35  
36  
37  
38  
39  
40  
41

### 42 5.3 Effects of pore and throat radii

43  
44 The influence of different pore-throat radii on the pressure field was investigated  
45 when considering the capillary and viscous forces using PNM-homo. The average  
46 pore-throat radii and corresponding permeability are listed in Table 5. These  
47 parameters were derived from the experiments with shale rocks (Lu et al., 2018). The  
48 sizes of simulation models for each pore radius are listed in Table 1.  
49  
50  
51  
52  
53  
54  
55  
56

57 Fig. 9(a) and (b) show the differences in the pressure fields between water and  
58 SC-CO<sub>2</sub> injections, respectively, in a homogeneous porous medium. Fig. 9(a) reveals  
59  
60  
61  
62  
63  
64  
65

1 that the values of DPDs varied for the different average pore-throat radii. The DPD  
2 was influenced by the geometries of pore and throat. Because the DPD occurred as a  
3 result of the capillary force, the simulation results indicate that the capillary force  
4 could not be neglected due to the low permeability of rock when the injection fluid  
5 (water) was immiscible with the formation fluid (oil).  
6  
7  
8  
9

10  
11  
12 By contrast, with the SC-CO<sub>2</sub> injection, no DPD occurred, as shown in Fig. 9(b).  
13  
14 The pressure field for the SC-CO<sub>2</sub> injection was controlled solely by the viscous force.  
15  
16 Because of the low viscosity of SC-CO<sub>2</sub>, the pressure distributions for different  
17 average pore-throat radii in small distances were nearly the same.  
18  
19  
20  
21  
22  
23

#### 24 5.4 Heterogeneous porous medium

25  
26 Rock for the most part is a heterogeneous porous media. Thus, investigating the  
27 pressure performances of water and SC-CO<sub>2</sub> injections in heterogeneous porous media  
28 is necessary. In our study, even the radius distributions were random, where the total  
29 average radius of the pore-throat for all pores and throats was 0.02  $\mu\text{m}$ . The  
30 corresponding sample sizes are listed in Table 1.  
31  
32  
33  
34  
35  
36  
37  
38

39  
40 A DPD occurred with water injection (Fig. 10(a)), but no DPD occurred with  
41 SC-CO<sub>2</sub> injection (Fig. 10(b)) in the heterogeneous porous medium. This indicated  
42 that the capillary and viscous forces affected the pressure fields in heterogeneous  
43 rocks. The results reveal that DPD clearly occurred when the injected fluid (water)  
44 was immiscible with the formation fluid (oil). For SC-CO<sub>2</sub>, the property of miscibility  
45 with hydrocarbon produces a strong seepage effect.  
46  
47  
48  
49  
50  
51  
52  
53  
54  
55  
56

#### 57 5.5 Well injection with pre-existing fracture

58  
59 Similar conditions as those in the experiment of Zhang et al. (Zhang et al., 2017)  
60  
61  
62  
63  
64  
65

1 were simulated using the PNM-frac. The formation fluid was assumed to be gas,  
2  
3 which was intended to represent shale gas rock (hydrocarbon wet). The average  
4  
5 pore-throat radius was set to 0.01  $\mu\text{m}$ . The simulation results of pressure distributions  
6  
7 for water and SC-CO<sub>2</sub> injections are presented in Fig. 11. The simulation results  
8  
9 revealed that the DPD derived from the capillary force between water and gas blocked  
10  
11 the spread of pressure (see Fig. 11(a)). However, in the case of SC-CO<sub>2</sub> injection,  
12  
13 pressure spread easily without blocks because of the absence of capillary forces, as  
14  
15 shown in Fig. 11(b). This indicated that the capillary force could cut off the pressure  
16  
17 when the injection pressure was insufficient to overcome the threshold of the capillary  
18  
19 force. It should be noted that the pore pressure in non-invaded elements in this model  
20  
21 was set to 0 MPa.  
22  
23  
24  
25  
26  
27  
28  
29  
30

## 31 5.6 Discussion of capillary force effect on the fracture geometry

32  
33 In general, fracturing with water leads to tensile failure, which in turn generates  
34  
35 fractures, and these fractures extend directly in the direction of the main stress. The  
36  
37 simulation results for water injection suggested that the pressure spread was blocked  
38  
39 by the capillary and viscous forces. However, the effect of capillary force on SC-CO<sub>2</sub>  
40  
41 injection was negligible, and the viscous force for SC-CO<sub>2</sub> injection was lower than  
42  
43 for water injection. The pressure could penetrate into the pore and throat around any  
44  
45 pre-existing fracture. This can cause the pore pressure to increase considerably as  
46  
47 compared with using water as injection fluid. When the pore pressure increased, the  
48  
49 effective stress decreased. If we consider the Mohr-Coulomb failure criterion, shear  
50  
51 failure events occur easily with a small effective stress (i.e., high pore pressure), as  
52  
53  
54  
55  
56  
57  
58  
59  
60  
61  
62  
63  
64  
65

1 shown in Fig.12(a). Therefore, increased pore pressure due to SC-CO<sub>2</sub> injection likely  
2  
3 initiates shear failure cracks. Typically, a crack caused by shear failure is not parallel  
4  
5 to a fracture caused by tensile failure (Labuz and Zang, 2012; Patton, 1966).  
6  
7 Fracturing due to SC-CO<sub>2</sub> injection may lead to more branched and high tortuous  
8  
9 fractures as well as rough fracture surfaces. Thus, the fracture geometry derived from  
10  
11 SC-CO<sub>2</sub> injection should be more complex than water injection because of shear  
12  
13 failure cracks (see Fig. 12(b)). These inferred behaviors are consistent with the  
14  
15 experimental results of Zhang et al., who showed that the fracture geometry of  
16  
17 SC-CO<sub>2</sub> was more complex than water fracturing.  
18  
19

20  
21  
22  
23  
24  
25 In fact, this paper is based on a flow model to study different pressure  
26  
27 performance when injecting water and SC-CO<sub>2</sub>. On this basis, combined with the  
28  
29 Mohr-Coulomb failure criterion, it is concluded that SC-CO<sub>2</sub> fracturing should induce  
30  
31 complex fracture. But this conclusion is not directly obtained through simulation.  
32  
33 Therefore, in the following work, we will develop a solid model and couple it with the  
34  
35 flow model to verify the aforementioned results that the fracture pattern induced by  
36  
37 SC-CO<sub>2</sub> fracturing is complex fracture networks.  
38  
39  
40  
41  
42  
43

## 44 6. Conclusion

45  
46  
47 A two-phase steady-state flow model considering the effects of capillary and  
48  
49 viscous forces was developed to investigate differences between aqueous and SC-CO<sub>2</sub>  
50  
51 injections. The results of this study can be summarized as follows.  
52  
53

54  
55 With respect to aqueous fluid injection, the pressure field was influenced by the  
56  
57 capillary force because of immiscibility. The capillary force produced DPDs at the  
58  
59  
60  
61  
62  
63  
64  
65

1 interfacial points. The effects of capillary force on aqueous fluid were significant with  
2  
3 respect to low-permeability reservoirs. However, miscible fluid such as SC-CO<sub>2</sub>  
4  
5 reduced the effect of the capillary force and prevented DPD. Miscibility with  
6  
7 hydrocarbon and the low viscosity of SC-CO<sub>2</sub> led to a strong seepage effect. The  
8  
9 strong seepage effect of SC-CO<sub>2</sub> increased pore pressure in wide areas and induced  
10  
11 shear fractures. This typically leads to the formation of complex fracture networks.  
12  
13  
14  
15  
16

## 17 **Acknowledgement**

18  
19 Thank you for previous researchers who use SC-CO<sub>2</sub> to be fracturing fluid and who  
20  
21 contributed to the development of PNM. Their research laid the foundation for my  
22  
23 research.  
24  
25  
26

## 27 **Author contributions**

28  
29 B. Liu planed and conducted the study. A. Suzuki contributed the design of the study.  
30  
31  
32 T. Ito contributed on the examination of the paper structure. All authors participated in  
33  
34 the discussion and interpretation of results, as well as the writing of the manuscript.  
35  
36  
37  
38

## 39 **Funding**

40  
41 This research did not receive any specific grant from funding agencies in the public,  
42  
43 commercial, or not-for-profit sectors.  
44  
45  
46

## 47 **Nomenclature**

48  
49  $g$  conductance,  $m^3/(\text{Pa}\cdot\text{s})$ ;  
50  
51

52  
53  $L$  length of an element,  $m$ ;  
54  
55

56  
57  $n$  number of corners;  
58

59  
60  $z$  number of elements connecting to element  $i$ ;  
61  
62  
63  
64  
65

1  $\alpha_i$  half corner angle at corner  $i$ ;  
2  
3  $P$  pressure, Pa;  
4  
5  
6  $P_c$  capillary pressure, Pa;  
7  
8  
9  $q$  volumetric flow rate,  $m^3/s$ ;  
10  
11  
12  $r$  the curvature radius of corner interface,  $m$ ;  
13  
14  
15  $R$  inscribed radius of a cross-section,  $m$ ;  
16  
17  $\Delta t$  time-step size,  $s$ ;  
18  
19  
20  $\theta$  contact angle, radian;  
21  
22  
23  $\sigma$  interfacial tension between two fluid phases,  $N/m$ ;  
24  
25  
26  $\mu$  fluid viscosity,  $Pa \cdot s$ ;  
27  
28  $V$  fluid volume in an element,  $m^3$ ;  
29  
30  
31  $nw$  non-wetting phase;  
32  
33  
34  $w$  wetting phase;  
35  
36  
37  $C$  conductance of fluid in cross section,  $Pa \cdot s/m^4$   
38  
39  $S_H, S_h$  Maximum principal stress and minimum principal stress  
40

## 41 **Reference**

- 42  
43  
44 Aker, E., JØrgen MÅlØy, K., Hansen, A., Batrouni, G.G., 1998. A two-dimensional  
45 network simulator for two-phase flow in porous media. *Transp. Porous Media* 32,  
46 163–186. <https://doi.org/10.1023/A:1006510106194>  
47  
48  
49  
50  
51  
52  
53 Al-Gharbi, M.S., 2004. Dynamic pore-scale modelling of two-phase flow. Imperial  
54 College London.  
55  
56  
57  
58 Al-Gharbi, M.S., Blunt, M.J., 2005. Dynamic network modeling of two-phase  
59  
60  
61  
62  
63  
64  
65

1 drainage in porous media. *Phys. Rev. E - Stat. Nonlinear, Soft Matter Phys.* 71,  
2  
3 1–16. <https://doi.org/10.1103/PhysRevE.71.016308>  
4  
5

6 Bakke, S., Øren, P.-E., 1997. 3-D Pore-scale modelling of sandstones and flow  
7  
8 simulations in the pore networks. *SPE J.* <https://doi.org/10.2118/35479-PA>  
9

10 Belytschko, T., Organ, D., Gerlach, C., 2000. Element-free galerkin methods for  
11  
12 dynamic fracture in concrete. *Comput. Methods Appl. Mech. Eng.* 187, 385–399.  
13  
14 [https://doi.org/10.1016/S0045-7825\(00\)80002-X](https://doi.org/10.1016/S0045-7825(00)80002-X)  
15  
16

17 Bennour, Z., Ishida, T., Nagaya, Y., Chen, Y., Nara, Y., Chen, Q., Sekine, K., Nagano,  
18  
19 Y., 2015. Crack extension in hydraulic fracturing of shale cores using viscous oil,  
20  
21 water, and liquid carbon dioxide. *Rock Mech. Rock Eng.* 48, 1463–1473.  
22  
23 <https://doi.org/10.1007/s00603-015-0774-2>  
24  
25

26 Blunt, M.J., 2001. Flow in porous media - pore-network models and multiphase flow.  
27  
28 *Curr. Opin. Colloid Interface Sci.*  
29  
30 [https://doi.org/10.1016/S1359-0294\(01\)00084-X](https://doi.org/10.1016/S1359-0294(01)00084-X)  
31  
32

33 Buckley, S.E., Leverett, M.C., 1942. Mechanism of fluid displacement in sands. *Trans.*  
34  
35 *AIME.* <https://doi.org/10.2118/942107-G>  
36  
37

38 Choo, L.Q., Zhao, Z., Chen, H., Tian, Q., 2016. Hydraulic fracturing modeling using  
39  
40 the discontinuous deformation analysis (DDA) method. *Comput. Geotech.* 76,  
41  
42 12–22. <https://doi.org/10.1016/j.compgeo.2016.02.011>  
43  
44  
45

46 Economides, M.J., Boney, C., 2000. Reservoir stimulation. *Reserv. Stimul.*  
47  
48 <https://doi.org/10.1017/CBO9781107415324.004>  
49  
50

51 Higdon, J.J.L., 2013. Multiphase flow in porous media. *J. Fluid Mech.*  
52  
53  
54  
55  
56  
57  
58  
59  
60  
61  
62  
63  
64  
65



1 <https://doi.org/10.1017/jfm.2013.296>

2  
3 Hughes, R.G., Blunt, M.J., 2000. Pore scale modeling of rate effects in imbibition.

4  
5  
6 Transp. Porous Media 40, 295–322. <https://doi.org/10.1023/A:1006629019153>

7  
8  
9 Idowu, N.A., Blunt, M.J., 2010. Pore-scale modelling of rate effects in waterflooding.

10  
11 Transp. Porous Media 83, 151–169. <https://doi.org/10.1007/s11242-009-9468-0>

12  
13  
14 Ishida, T., Chen, Y., Bennour, Z., Yamashita, H., Inui, S., Nagaya, Y., Naoi, M., Chen,

15  
16 Q., Nakayama, Y., Nagano, Y., 2016a. Features of CO<sub>2</sub> fracturing deduced from

17  
18 acoustic emission and microscopy in laboratory experiments. J. Geophys. Res.

19  
20  
21 Solid Earth 121, 8080–8098. <https://doi.org/10.1002/2016JB013365>

22  
23  
24  
25 Ishida, T., Chen, Y., Bennour, Z., Yamashita, H., Inui, S., Nagaya, Y., Naoi, M., Chen,

26  
27 Q., Nakayama, Y., Nagano, Y., 2016b. Features of CO<sub>2</sub> fracturing deduced from

28  
29 acoustic emission and microscopy in laboratory experiments. J. Geophys. Res.

30  
31  
32 Solid Earth. <https://doi.org/10.1002/2016JB013365>

33  
34  
35  
36 Joekar-Niasar, V., Hassanizadeh, S.M., 2012. Analysis of fundamentals of two-phase

37  
38 flow in porous media using dynamic pore-network models: A review. Crit. Rev.

39  
40  
41 Environ. Sci. Technol. 42, 1895–1976.

42  
43  
44 <https://doi.org/10.1080/10643389.2011.574101>

45  
46  
47 Kantzas, Apostolos; Bryan Jonathan; Taheri, S., 2015. Fundamentals of fluid flow in

48  
49 porous media 336.

50  
51  
52 Labuz, J.F., Zang, A., 2012. Mohr-Coulomb failure criterion. Rock Mech. Rock Eng.

53  
54  
55 <https://doi.org/10.1007/s00603-012-0281-7>

56  
57  
58 Latham, J., Guo, L., Wang, X., Xiang, J., 2011. Modelling the evolution of fractures

59  
60  
61  
62  
63  
64  
65

1 using a combined FEM-DEM numerical method. *Harmon. Rock Eng. Environ.*

2  
3 449–454. <https://doi.org/10.1201/b11646-77>

4  
5  
6 Lecampion, B., Bungler, A., Zhang, X., 2017. Numerical methods for hydraulic

7  
8 fracture propagation: A review of recent trends. *J. Nat. Gas Sci. Eng.*

9  
10 <https://doi.org/10.1016/j.jngse.2017.10.012>

11  
12  
13  
14 Liu, Q., Sun, L., Liu, P., Chen, L., 2018. Modeling simultaneous multiple fracturing

15  
16 using the combined finite-discrete element method. *Geofluids* 2018.

17  
18  
19 <https://doi.org/10.1155/2018/4252904>

20  
21  
22  
23 Lu, S., Li, J., Zhang, P., Xue, H., Wang, G., Zhang, J., Liu, H., Li, Z., 2018.

24  
25 Classification of microscopic pore-throats and the grading evaluation on shale oil

26  
27 reservoirs. *Pet. Explor. Dev.* 45, 452–460.

28  
29  
30 [https://doi.org/10.1016/S1876-3804\(18\)30050-8](https://doi.org/10.1016/S1876-3804(18)30050-8)

31  
32  
33  
34 Middleton, R., Viswanathan, H., Currier, R., Gupta, R., 2014. CO<sub>2</sub> as a fracturing

35  
36 fluid: Potential for commercial-scale shale gas production and CO<sub>2</sub> sequestration.

37  
38  
39 *Energy Procedia* 63, 7780–7784. <https://doi.org/10.1016/j.egypro.2014.11.812>

40  
41  
42 Mogensen, K., Stenby, E.H., 1998. A dynamic two-phase pore-scale model of

43  
44 imbibition. *Transp. Porous Media* 32, 299–327.

45  
46  
47 <https://doi.org/10.1023/a:1006578721129>

48  
49  
50 Nguyen, V.H., Sheppard, A.P., Knackstedt, M.A., Val Pinczewski, W., 2006. The

51  
52 effect of displacement rate on imbibition relative permeability and residual

53  
54 saturation. *J. Pet. Sci. Eng.* 52, 54–70.

55  
56  
57 <https://doi.org/10.1016/j.petrol.2006.03.020>

58  
59  
60  
61  
62  
63  
64  
65

- 1 Øren, P.E., Bakke, S., 2003. Reconstruction of Berea sandstone and pore-scale  
2  
3 modelling of wettability effects. *J. Pet. Sci. Eng.*  
4  
5  
6 [https://doi.org/10.1016/S0920-4105\(03\)00062-7](https://doi.org/10.1016/S0920-4105(03)00062-7)  
7  
8
- 9 Øren, P.E., Bakke, S., 2002. Process based reconstruction of sandstones and  
10  
11 prediction of transport properties. *Transp. Porous Media.*  
12  
13  
14 <https://doi.org/10.1023/A:1015031122338>  
15  
16
- 17 Patton, F.D., 1966. Multiple modes of shear failure in rock. 1st Int. Congr. Rock  
18  
19 Mech.  
20  
21
- 22 Peng, P., Ju, Y., Wang, Y., Wang, S., Gao, F., 2017. Numerical analysis of the effect  
23  
24 of natural microcracks on the supercritical CO<sub>2</sub> fracturing crack network of shale rock  
25  
26 based on bonded particle models. *Int. J. Numer. Anal. Methods Geomech.*  
27  
28  
29 <https://doi.org/10.1002/nag.2712>  
30  
31
- 32 Piri, M., Blunt, M.J., 2005. Three-dimensional mixed-wet random pore-scale network  
33  
34 modeling of two- And three-phase flow in porous media. I. Model description.  
35  
36  
37 *Phys. Rev. E - Stat. Nonlinear, Soft Matter Phys.* 71, 1–30.  
38  
39  
40 <https://doi.org/10.1103/PhysRevE.71.026301>  
41  
42
- 43 Reynolds, C.A., Blunt, M.J., Krevor, S., 2018. Multiphase Flow Characteristics of  
44  
45 Heterogeneous Rocks From CO<sub>2</sub> Storage Reservoirs in the United Kingdom.  
46  
47  
48 *Water Resour. Res.* <https://doi.org/10.1002/2017WR021651>  
49  
50
- 51 Shi, F., Wang, X.L., Liu, C., Liu, H., Wu, H.A., 2017. An XFEM-based method with  
52  
53 reduction technique for modeling hydraulic fracture propagation in formations  
54  
55  
56 containing frictional natural fractures. *Eng. Fract. Mech.* 173, 64–90.  
57  
58  
59  
60  
61  
62  
63  
64  
65

- 1 Shimizu, H., Murata, S., Ishida, T., 2011. The distinct element analysis for hydraulic  
2  
3 fracturing in hard rock considering fluid viscosity and particle size distribution.  
4  
5  
6 Int. J. Rock Mech. Min. Sci. 48, 712–727.  
7  
8  
9 <https://doi.org/10.1016/j.ijrmms.2011.04.013>  
10
- 11 Valvatne, H., 2004. Predictive pore-scale modelling of multiphase flow 146.  
12
- 13 Vilarrasa, V., Bolster, D., Dentz, M., Olivella, S., Carrera, J., 2010. Effects of CO<sub>2</sub>  
14  
15 compressibility on CO<sub>2</sub> storage in deep saline aquifers. Transp. Porous Media.  
16  
17  
18  
19 <https://doi.org/10.1007/s11242-010-9582-z>  
20  
21
- 22 Wang, S., Feng, Q., Dong, Y., Han, X., Wang, S., 2015. A dynamic pore-scale  
23  
24 network model for two-phase imbibition. J. Nat. Gas Sci. Eng. 26, 118–129.  
25  
26  
27  
28 <https://doi.org/10.1016/j.jngse.2015.06.005>  
29  
30
- 31 Watanabe, N., Egawa, M., Sakaguchi, K., Ishibashi, T., Tsuchiya, N., 2017. Hydraulic  
32  
33 fracturing and permeability enhancement in granite from subcritical/brittle to  
34  
35  
36 supercritical/ductile conditions. Geophys. Res. Lett. 44, 5468–5475.  
37  
38  
39 <https://doi.org/10.1002/2017GL073898>  
40  
41
- 42 Yan, C., Zheng, H., Sun, G., Ge, X., 2016. Combined finite-discrete element method  
43  
44 for simulation of hydraulic fracturing. Rock Mech. Rock Eng. 49, 1389–1410.  
45  
46  
47  
48 <https://doi.org/10.1007/s00603-015-0816-9>  
49
- 50 Zhang, X., Lu, Y., Tang, J., Zhou, Z., Liao, Y., 2017. Experimental study on fracture  
51  
52 initiation and propagation in shale using supercritical carbon dioxide fracturing.  
53  
54  
55  
56 Fuel 190, 370–378. <https://doi.org/10.1016/j.fuel.2016.10.120>  
57
- 58 Zhao, Q., Lisjak, A., Mahabadi, O., Liu, Q., Grasselli, G., 2014. Numerical simulation  
59  
60  
61  
62  
63  
64  
65

1 of hydraulic fracturing and associated microseismicity using finite-discrete  
2  
3 element method. *J. Rock Mech. Geotech. Eng.* 6, 574–581.  
4

5  
6 <https://doi.org/10.1016/j.jrmge.2014.10.003>  
7  
8  
9  
10  
11  
12  
13  
14  
15  
16  
17  
18  
19  
20  
21  
22  
23  
24  
25  
26  
27  
28  
29  
30  
31  
32  
33  
34  
35  
36  
37  
38  
39  
40  
41  
42  
43  
44  
45  
46  
47  
48  
49  
50  
51  
52  
53  
54  
55  
56  
57  
58  
59  
60  
61  
62  
63  
64  
65

1                    **Estimating the Seepage Effect of SC-CO<sub>2</sub> and Water Fracturing with a**  
2  
3                    **Steady-state Flow Model: Consider Capillary and Viscous Forces in Pore Scale**  
4

5  
6                    Bailong Liu, Anna Suzuki, and Takatoshi Ito  
7

8  
9                    Institute of Fluid Science, Tohoku University., Japan  
10

11                    **Abstract**  
12

13  
14                    Supercritical carbon dioxide (SC-CO<sub>2</sub>) fracturing is a promising technology for  
15                    unconventional energy development and carbon capture and storage. Experimental  
16                    studies have shown that SC-CO<sub>2</sub> fracturing can form complex fracture networks and  
17                    reduce crack initiation pressure, which are different results from those when  
18                    fracturing with aqueous fluids. The complex fracture networks that form from  
19                    SC-CO<sub>2</sub> fracturing may be the result of the strong seepage effect (i.e., low capillary  
20                    and viscous forces). To understand the different injection behaviors induced by  
21                    SC-CO<sub>2</sub> and aqueous fluids in low-permeability rocks, this study develops a new  
22                    two-phase steady-state model based on the pore-scale network method. Although  
23                    other models consider the viscous force, our model implements the capillary and  
24                    viscous forces to reproduce the seepage effect. Because of the capillary force, the flow  
25                    model is nonlinear and solved by iteratively solving matrix equations until a  
26                    conservation of volumetric flux is satisfied. Simulation results show that the capillary  
27                    force in a two-phase flow is not negligible on pressure distribution in small pore  
28                    spaces. This leads to discontinuous pressure drops. This study shows that the seepage  
29                    effect of SC-CO<sub>2</sub> is stronger than that of aqueous fluids.  
30  
31  
32  
33  
34  
35  
36  
37  
38  
39  
40  
41  
42  
43  
44  
45  
46  
47  
48  
49  
50  
51  
52  
53  
54  
55  
56  
57

58                    **Keyword: Seepage effect; SC-CO<sub>2</sub> fracturing; Shale rock; Pore scale network**  
59  
60  
61  
62  
63  
64  
65

1 **model**

2  
3 **1. Introduction**

4  
5  
6 Supercritical carbon dioxide (SC-CO<sub>2</sub>) is a special fluid with a low viscosity  
7  
8 (like gas) and high density (like liquid). Experimental studies have shown that  
9  
10 SC-CO<sub>2</sub> has many potential advantages as a fracturing fluid. For instance, SC-CO<sub>2</sub>  
11  
12 fracturing reduces initiation pressure by 50% or more (Zhang et al., 2017). Fractures  
13  
14 induced by SC-CO<sub>2</sub> are irregular multiple cracks and easily form complex fracture  
15  
16 networks, which are different from fractures induced by conventional aqueous fluids  
17  
18 (Bennour et al., 2015; Ishida et al., 2016a; Zhang et al., 2017). These characteristics  
19  
20 of SC-CO<sub>2</sub> fracturing yield positive effects on unconventional energy developments,  
21  
22 including CO<sub>2</sub> sequestration and enhanced geothermal systems (Middleton et al., 2014;  
23  
24 Reynolds et al., 2018).

25  
26  
27  
28  
29  
30  
31  
32  
33  
34 Injected water can be an immiscible fluid in oil and gas reservoirs, whereas  
35  
36 injected SC-CO<sub>2</sub> can be a miscible fluid. When comparing water injection and  
37  
38 SC-CO<sub>2</sub> injection, two-phase flow should be considered. In addition, the different  
39  
40 performances of SC-CO<sub>2</sub> fracturing from aqueous fluid fracturing are generally  
41  
42 considered to derive from the strong seepage effects of SC-CO<sub>2</sub> (Ishida et al., 2016;  
43  
44 Watanabe et al., 2017; Zhang et al., 2017). The seepage effect may be influenced by  
45  
46 capillary and viscous forces in small pore spaces in a two-phase flow (Kantzas,  
47  
48 Apostolos; Bryan Jonathan; Taheri, 2015). Strong seepage effects occur because of  
49  
50 low viscous and low capillary forces, which often lead to increased percolation and  
51  
52 increased pore pressure. Some studies have investigated pore pressure distribution  
53  
54  
55  
56  
57  
58  
59  
60  
61  
62  
63  
64  
65

1 during fracturing, but their flow models have considered only the viscous force  
2  
3 (Belytschko et al., 2000; Choo et al., 2016; Economides and Boney, 2000; Latham et  
4  
5 al., 2011; Lecampion et al., 2017; Liu et al., 2018; Peng et al., 2017; Shi et al., 2017;  
6  
7 Shimizu et al., 2011; Yan et al., 2016; Zhao et al., 2014). The capillary force cannot be  
8  
9 ignored in low-permeability porous media such as shale rock when a two-phase flow  
10  
11 occurs (Blunt, 2001; Higdon, 2013).  
12  
13  
14  
15  
16

17 The pore-scale network model (PNM) has been developed to simulate flow in  
18  
19 porous media (Valvatne, 2004), and some studies have simulated the multiphase flow  
20  
21 in the pore scale using a PNM (Al-Gharbi and Blunt, 2005; Joekar-Niasar and  
22  
23 Hassanizadeh, 2012; Wang et al., 2015). Because a PNM can consider small pore  
24  
25 geometries, it is used to closely examine behaviors in the pore space.  
26  
27  
28  
29  
30

31 In this study, a two-phase steady-state flow model is developed to investigate the  
32  
33 seepage effects of SC-CO<sub>2</sub>. The model integrates both capillary and viscous forces  
34  
35 based on the PNM. We analyze the characteristics of the pressure field during fluid  
36  
37 injection, which directly influence fracture geometries during fracturing. In addition,  
38  
39 the difference between injection SC-CO<sub>2</sub> and injection water is discussed.  
40  
41  
42  
43  
44

## 45 **2. Model description**

### 46 **2.1 Pore-scale network models**

47  
48 The PNM is an effective model to represent flow in a porous medium through the  
49  
50 pores and throats. In the fracturing process, injection fluid is pushed into formations,  
51  
52 and the formation fluid is displaced. In general, three types of displacements can  
53  
54 occur during fracturing: piston-like, pore-body filling, or snap-off (Valvatne, 2004).  
55  
56  
57  
58  
59  
60  
61  
62  
63  
64  
65



1 The piston-like displacement refers to invasion into throats by fluid that were  
2  
3 previously present in pores. In a pore-body filling displacement, fluid in pores is  
4  
5 displaced by the fluid in throats. Snap-off displacement describes invasion by wetting  
6  
7 fluid at the corner of a cross section when the pressure of the invasion fluid is lower  
8  
9 than the threshold of the capillary pressure. The effect of snap-off displacement is  
10  
11 known to be considerably smaller than the effects of the other two types of  
12  
13 displacements in shale rocks (Al-Gharbi and Blunt, 2005). Thus, the current model  
14  
15 considers only piston-like displacement and pore-body filling. In our network model,  
16  
17 the triangular cross section was selected to consider the wetting phase flow (film flow)  
18  
19 at the corners (Mogensen and Stenby, 1998; Nguyen et al., 2006).

27  
28 Let us consider that there are two adjacent elements  $i$  and  $j$ . (Note that whether  
29  
30 they are pores or throats is irrelevant.) The flow rate from element  $i$  to element  $j$ ,  
31  
32  $q_{ij}$ , is given by:

$$33$$

$$34 \quad q_{ij} = g_{ij}(P_i - P_j + P_{c,ij}) \#(1)$$

$$35$$

36  
37 where  $g_{ij}$  is the flow conductivity between elements  $i$  and  $j$ .  $P_i$  and  $P_j$  are the  
38  
39 pressures for elements  $i$  and  $j$ , respectively.  $P_{c,ij}$  is the capillary force between  
40  
41 elements  $i$  and  $j$ . The flow conductivity equations are given by (Hughes and Blunt,  
42  
43  
44  
45  
46  
47 2000):

$$48$$

$$49 \quad g_{ij} = \int_0^L g(x) dx \#(2)$$

$$50$$

$$51$$

$$52 \quad g(x) = 1/C(x), 0 \leq x \leq L \#(3)$$

$$53$$

54  
55 where  $\mu$  is the fluid viscosity,  $L$  is the length between elements  $i$  and  $j$ , and  $C(x)$   
56  
57 is the fluid conductance per unit length and is determined by the fluid configuration in  
58  
59  
60  
61  
62  
63  
64  
65

1 their cross sections.

2  
3 Two types of cross-section configurations (see Fig. 1(a)) can be generated when  
4 the injection fluid is different from the formation fluid: single-phase configuration (in  
5 a non-invaded element),  $C_{sp}$ ; and two-phase configuration (in an invaded element),  
6  $C_{tp}$ . The geometric parameters for calculating conductance and area are shown in Fig.  
7  
8  
9  
10  
11  
12  
13  
14  
15  
16  
17  
18  
19  
20  
21  
22  
23  
24  
25  
26  
27  
28  
29  
30  
31  
32  
33  
34  
35  
36  
37  
38  
39  
40  
41  
42  
43  
44  
45  
46  
47  
48  
49  
50  
51  
52  
53  
54  
55  
56  
57  
58  
59  
60  
61  
62  
63  
64  
65

For single-phase configuration, the fluid conductance per unit length,  $C_{sp}$ , is given by (Aker et al., 1998; Al-Gharbi, 2004):

$$C_{sp} = \frac{\pi\mu_w}{128} \left( R + (A_t/\pi)^{\frac{1}{2}} \right)^4 \quad \#(4)$$

where  $A_t$  is the cross-section area of the element and  $R$  is the inscribed radius of the cross section. The cross-section area of the element,  $A_t$ , is:

$$A_t = R^2 \sum_{i=1}^n \cot \alpha_i \quad \#(5)$$

where  $\alpha_i$  is the half corner angle and  $n$  is the number of corners in the cross section.

For two-phase configuration, the wetting and non-wetting phases in the cross section should be considered. The fluid conductance per unit length for the two-phase configuration,  $C_{tp}$ , is described by:

$$C_{tp} = (C_{nw} + C_w) / C_{nw} C_w \quad \#(6)$$

where  $C_{nw}$  and  $C_w$  represent the conductance of the non-wetting phase and wetting phase fluids in the center and at the corner, respectively, which is given by (Aker et al., 1998; Al-Gharbi, 2004):

$$C_{nw} = \frac{\pi\mu_{nw}}{128} \left( R + (A_{nw}/\pi)^{\frac{1}{2}} \right)^4 \quad \#(7)$$

$$C_w = \mu_w \sum_{i=1}^n \left( \frac{A_{ci}(1 - \sin \alpha_i)\varphi_3}{\sin \alpha_i (1 - \varphi_3)(\varphi_2 + f\varphi_1)} \cdot \left( \frac{\varphi_2 \cos \theta - \varphi_1}{12} \right)^{\frac{1}{2}} \right)^2 \#(8)$$

The parameters  $\varphi_1$ ,  $\varphi_2$ , and  $\varphi_3$  depend on the half corner angle  $\alpha$  and the contact angle  $\theta$ . The parameter  $f$  indicates the capacity of fluid crossing the fluid interface (Piri and Blunt, 2005). In our model, the parameter  $f$  equals 1, which means that no flow occurs on the fluid interface. The area of the formation fluid (wetting phase fluid) at the corner,  $A_w$ , and injection fluid (non-wetting phase fluid) at the center,  $A_{nw}$ , are calculated by:

$$A_w = \sum_{i=1}^n A_{ci} \#(9)$$

$$A_{ci} = r^2 \left( \cos \theta (\cot \alpha_i \cos \theta - \sin \theta) + \theta + \alpha_i - \frac{\pi}{2} \right) \#(10)$$

$$A_{nw} = A_t - A_w \#(11)$$

where  $r$  is the radius of the curvature of the interface.

For elements invaded by injection fluid (see Fig. 1(b)), the flow rate  $q_{ij}$  as given in the following equation is divided into the flow rates of the wetting and non-wetting phases as:

$$q_{ij} = q_{nw,ij} + q_{w,ij} \#(12)$$

The flow rate of each phase from element  $i$  to element  $j$  is given by:

$$q_{nw,ij} = q_{ij} C_{nw,i} / (C_{nw,i} + C_{w,i}) \#(13)$$

$$q_{w,ij} = q_{ij} C_{w,i} / (C_{nw,i} + C_{w,i}) \#(14)$$

where  $C_{w,i}$  and  $C_{nw,i}$  represent the conductance of the non-wetting and wetting phase fluids in element  $i$ , respectively.

The capillary force ( $P_{c,ij}$ ) between element  $i$  and  $j$  is calculated using the

1 Young–Laplace equation:

$$2 \quad 3 \quad 4 \quad 5 \quad 6 \quad 7 \quad 8 \quad 9 \quad 10 \quad 11 \quad 12 \quad 13 \quad 14 \quad 15 \quad 16 \quad 17 \quad 18 \quad 19 \quad 20 \quad 21 \quad 22 \quad 23 \quad 24 \quad 25 \quad 26 \quad 27 \quad 28 \quad 29 \quad 30 \quad 31 \quad 32 \quad 33 \quad 34 \quad 35 \quad 36 \quad 37 \quad 38 \quad 39 \quad 40 \quad 41 \quad 42 \quad 43 \quad 44 \quad 45 \quad 46 \quad 47 \quad 48 \quad 49 \quad 50 \quad 51 \quad 52 \quad 53 \quad 54 \quad 55 \quad 56 \quad 57 \quad 58 \quad 59 \quad 60 \quad 61 \quad 62 \quad 63 \quad 64 \quad 65$$

$$P_{c,ij} = \frac{2\sigma \cos \theta}{r} \#(15)$$

where  $\sigma$  denotes interfacial tension between the two fluid phases.

Considering the small compressibility of SC-CO<sub>2</sub> (Vilarrasa et al., 2010), the conservation equation is applicable to SC-CO<sub>2</sub> flow. For either single- or two-phase flow, the conservation of the volume flux at element  $i$  can be described by:

$$\sum_{j=1}^{Z_i} q_{ij} = \sum_{j=1}^{Z_i} (q_{nw,ij} + q_{w,ij}) = 0 \#(16)$$

where  $Z_i$  is the number of elements connecting to element  $i$ . For instance, the pore  $i$  connects throats 1–3 in Fig. 2. The conservation of volume flux at pore  $i$  can be expressed as  $q_{i2} + q_{i3} + q_{i1} = 0$ .

Each pore connects more than one throat in our numerical model. Based on the flow rate of (1) – (16) and the topological structure of the network, the assembly equation can be formed as:

$$\begin{bmatrix} D_{11} & \cdots & D_{1j} \\ \vdots & \ddots & \vdots \\ D_{i1} & \cdots & D_{ij} \end{bmatrix} \begin{Bmatrix} P_1 \\ \vdots \\ P_i \end{Bmatrix} = \begin{Bmatrix} \sum_{j=1}^{Z_1} g_{1j} P_{c,1j} \\ \vdots \\ \sum_{j=1}^{Z_i} g_{ij} P_{c,ij} \end{Bmatrix} \#(17)$$

where  $D_{ij}$  is the conductance matrix. When  $i = j$ ,  $D_{ij} = \sum_{j=1}^{Z_i} g_{ij}$ ; otherwise,  $D_{ij} = g_{ij}$ .

## 2.2 Computational procedure

Based on the previous discussion, we derived the quasi-steady-state pressure distribution. To simulate fluid injection, a time variation of the fluid flow was calculated. We iterated to obtain the steady-state pressure distribution at each time

1 step  $\Delta t$ . The computational procedure, as shown in Fig. 3, is described as follows:

2  
3  
4 1) Based on the initial condition, the conductivity of each element is calculated by  
5  
6 using (4) – (11). Then, the integral conductance matrix  $D_{ij}$  and force matrix are  
7  
8 assembled.

9  
10  
11 2) As  $P_{outlet}^t$  and  $P_{inlet}^t$  are known, the pressure distribution is obtained from (17).  
12  
13 Based on the pressure distribution, the total flow rate  $q_{ij}$ , the non-wetting phase flow  
14  
15 rate  $q_{nw,ij}$ , and the wetting phase flow rate  $q_{w,ij}$  can be solved through (1) and (12) –  
16  
17 (14).  
18  
19

20  
21  
22 3) Calculate each phase fluid volume  $V_{w,i}^{t+\Delta t}$  and  $V_{nw,i}^{t+\Delta t}$  in element  $i$  at  $t + \Delta t$  by  
23  
24 using (18) – (19). Update the meniscus position and fluid configuration of each  
25  
26 element based on each phase fluid volume. The purpose of choosing  $\Delta t$  is to ensure  
27  
28 every meniscus will not cross one throat element in  $\Delta t$ . Then, the initial condition can  
29  
30 be updated according to the configuration at  $t + \Delta t$ .  
31  
32

33  
34  
35 The volume of each of the wetting and non-wetting phases in element  $i$  can be  
36  
37 expressed by:  
38  
39

40  
41  
42 
$$V_{w,i}^{t+\Delta t} = V_{w,i}^t + \Delta t \times \sum_{j=1}^{Z_i} q_{w,ij} \#(18)$$

43  
44  
45 
$$V_{nw,i}^{t+\Delta t} = V_{nw,i}^t + \Delta t \times \sum_{j=1}^{Z_i} q_{nw,ij} \#(19)$$

46  
47  
48  
49 **3. Simulation condition**

50  
51  
52 We simulated seepage effects (capillary and viscous forces) for SC-CO<sub>2</sub> and  
53  
54 water fracturing as previously examined in the SC-CO<sub>2</sub> and water fracturing  
55  
56 experiment conducted by Zhang et al (Zhang et al., 2017).  
57  
58  
59  
60  
61  
62  
63  
64  
65

### 3.1 Structure of PNM

Two pore network structures were used in the simulation cases. One structure, labeled Network A, was used to validate the flow model and investigate the difference between injecting SC-CO<sub>2</sub> and water, as shown in Fig. 4(a). Network A was used to represent two types of porous media: homogenous porous medium (PNM-homo) and heterogeneous porous medium (PNM-hetero). For PNM-homo, a constant average radius of pores and throats was set for a single simulation. To investigate the effects of different radii, the radii of pores and throats varied from 0.01 to 0.15  $\mu\text{m}$  for each simulation. Thus, the sizes of the simulation models varied for different average radii of pores and throats, see Table 1. The lengths were normalized by the size of each simulation model. For PNM-hetero, the distributions of radii of throats and pores were generated based on the statistical data of sandstone (Bakke and Øren, 1997; Øren and Bakke, 2003, 2002), which is shown in Fig. 5. The other structure, Network B, was assumed to contain a pre-existing fracture (PNM-frac), which was to see pressure distribution around fracture. (see Fig. 4(b)). The size of Network B was consistent with the experimental sample of Zhang et al. (Zhang et al., 2017).

### 3.2 Fluid parameter and injection pressure

Four fluid systems and fluid viscosities, as listed in Tables 2 and 3, respectively, were used in the simulation and considered in the discussion. The formation fluid was gas or oil and the injection fluid was oil, water, or SC-CO<sub>2</sub>. SC-CO<sub>2</sub> is miscible with hydrocarbons and has a high diffusion coefficient. In the fracturing process, a pressurization stage occurs before crack initiation. At this pressurization stage, SC-CO<sub>2</sub> can fully dissolve with the formation fluid at the interface area. The interface between SC-CO<sub>2</sub> and hydrocarbon (gas or oil) disappears and the capillary force

1 decreases to zero. Before SC-CO<sub>2</sub> dissolves sufficiently into a formation fluid, the  
2  
3 interfacial tension between SC-CO<sub>2</sub> and hydrocarbon is very small, approximately 2  
4  
5 mN/m (Li et al., 2017). The interfacial tension between water and hydrocarbon is  
6  
7 approximately 50 mN/m. Thus, our simulation assumed that the capillary force  
8  
9 between SC-CO<sub>2</sub> and the formation fluids (oil or gas) was negligible.  
10  
11  
12

13  
14 The inlet and outlet pressure values were derived from the fracturing  
15  
16 experimental conditions of Zhang et al. (Zhang et al., 2017). In their experiment, the  
17  
18 injection pressure was approximately 5 MPa after fracture initiation. Considering the  
19  
20 pressure loss in tube, 4 MPa was used as the inlet pressure. However, 8 MPa was also  
21  
22 set as the inlet pressure to ensure that the inlet pressure was higher than the threshold  
23  
24 of the capillary force for different radii.  
25  
26  
27  
28  
29

#### 30 **4. Validation**

31  
32 A validation of the flow model was conducted by comparing the analytical  
33  
34 solutions in different flow situations: a) single-phase flow (the injection and formation  
35  
36 fluids were the same); b) two-phase flow without considering the capillary force ( $P_c$ ).  
37  
38 The analytical solutions were based on the Buckley-Leverett theory (Buckley and  
39  
40 Leverett, 1942; Idowu and Blunt, 2010). These solutions and the numerical results  
41  
42 obtained from the flow model are plotted in Fig. 6. The numerical results of the  
43  
44 single- and two-phase flows without capillary force were confirmed to be in good  
45  
46 agreement with the analytical results derived from the homogeneous porous medium.  
47  
48  
49  
50  
51  
52  
53  
54

#### 55 **5. Simulation and results**

56  
57 To investigate the seepage effects of SC-CO<sub>2</sub> injection, five simulations were  
58  
59  
60  
61  
62  
63  
64  
65

1 conducted. Both capillary and viscous forces were integrated into the PNM to  
2  
3 simulate the pressure field for a two-phase flow. The different injection conditions are  
4  
5 listed in [Table 4](#).  
6  
7

### 8 9 **5.1 Effects of capillary force**

10  
11 The effects of capillary force on two-phase flow are presented in [Fig. 7](#). The  
12  
13 PNM-homo was used to simulate the effect of the capillary force. The constant  
14  
15 pore-throat radius was set to  $0.1 \mu m$ . The results yielded snapshots of the pressure  
16  
17 distributions derived from water injection with and without capillary force. Water was  
18  
19 injected from the inlet (normalized length = 0). The case without  $P_c$  only considered  
20  
21 the effect of viscous force, whereas that with  $P_c$  considered the effects of both  
22  
23 capillary and viscous forces. When the capillary force was considered, a  
24  
25 discontinuous pressure drop (DPD) occurred. The capillary force posed an extra  
26  
27 resistant force to block the invasion of water. This resistant force derived from the  
28  
29 capillary force could cause a DPD in the two-phase flow.  
30  
31  
32  
33  
34  
35  
36  
37  
38

### 39 **5.2 Effects of injection time**

40  
41  
42 Water or SC-CO<sub>2</sub> injections were simulated in a homogeneous porous medium  
43  
44 using PNM-homo. The constant average pore-throat radius was  $0.1 \mu m$ . The time  
45  
46 variation of the pressure field is shown in [Fig. 8](#). Water or SC-CO<sub>2</sub> was injected from  
47  
48 the inlet (normalized length = 0), and the pressure field of the water injection, as  
49  
50 shown in [Fig.8\(a\)](#), experienced a DPD that was caused by the capillary force. The  
51  
52 injection fluid (water) was immiscible with the formation fluid (oil). When they met  
53  
54 during injection, the capillary force was generated at the interface between water and  
55  
56  
57  
58  
59  
60  
61  
62  
63  
64  
65



1 oil. With continuous injection, DPD continuously affected the pressure field. The  
2  
3 positions of the DPD moved to the outlet side because of changes in the interfacial  
4  
5  
6 position between water and oil.  
7

8  
9 By contrast, the pressure field of the SC-CO<sub>2</sub> injection experienced no DPD, as  
10  
11 shown in Fig. 8(b). Because SC-CO<sub>2</sub> and oil are miscible, no interface existed  
12  
13 between them. In other words, no capillary force occurred between SC-CO<sub>2</sub> and oil,  
14  
15 which means that no DPD occurred. Fig. 8(b) also shows that the slope of the pressure  
16  
17 curve in the area displaced by SC-CO<sub>2</sub> (inlet side) was flatter than the area occupied  
18  
19 by oil (outlet side). This was caused by both low viscous and low capillary forces of  
20  
21 SC-CO<sub>2</sub>, (i.e., the seepage effect). Because the injected SC-CO<sub>2</sub> penetrated into pores  
22  
23 easily given a small pressure drop, pressure propagation was advanced with a value  
24  
25 that approximated the injection pressure. The change points of slopes could be  
26  
27 considered the interfacial positions between SC-CO<sub>2</sub> and oil. The interfacial position  
28  
29 between SC-CO<sub>2</sub> and oil was ahead of that between water and oil. This indicated that  
30  
31 the seepage effect of SC-CO<sub>2</sub> promoted the advancement of the interfacial front.  
32  
33  
34  
35  
36  
37  
38  
39  
40

### 41 **5.3 Effects of pore and throat radii**

42  
43  
44 The influence of different pore-throat radii on the pressure field was investigated  
45  
46 when considering the capillary and viscous forces using PNM-homo. The average  
47  
48 pore-throat radii and corresponding permeability are listed in Table 5. These  
49  
50 parameters were derived from the experiments with shale rocks (Lu et al., 2018). The  
51  
52 sizes of simulation models for each pore radius are listed in Table 1.  
53  
54  
55

56  
57 Fig. 9(a) and (b) show the differences in the pressure fields between water and  
58  
59 SC-CO<sub>2</sub> injections, respectively, in a homogeneous porous medium. Fig. 9(a) reveals  
60  
61  
62  
63  
64  
65

1 that the values of DPDs varied for the different average pore-throat radii. The DPD  
2 was influenced by the geometries of pore and throat. Because the DPD occurred as a  
3 result of the capillary force, the simulation results indicate that the capillary force  
4 could not be neglected due to the low permeability of rock when the injection fluid  
5 (water) was immiscible with the formation fluid (oil).  
6  
7  
8  
9  
10

11  
12 By contrast, with the SC-CO<sub>2</sub> injection, no DPD occurred, as shown in [Fig. 9\(b\)](#).  
13 The pressure field for the SC-CO<sub>2</sub> injection was controlled solely by the viscous force.  
14 Because of the low viscosity of SC-CO<sub>2</sub>, the pressure distributions for different  
15 average pore-throat radii in small distances were nearly the same.  
16  
17  
18  
19  
20  
21

#### 22 **5.4 Heterogeneous porous medium**

23  
24 Rock for the most part is a heterogeneous porous media. Thus, investigating the  
25 pressure performances of water and SC-CO<sub>2</sub> injections in heterogeneous porous media  
26 is necessary. In our study, even the radius distributions were random, where the total  
27 average radius of the pore-throat for all pores and throats was 0.02  $\mu\text{m}$ . The  
28 corresponding sample sizes are listed in [Table 1](#).  
29  
30  
31  
32  
33  
34  
35  
36  
37  
38

39  
40 A DPD occurred with water injection ([Fig. 10\(a\)](#)), but no DPD occurred with  
41 SC-CO<sub>2</sub> injection ([Fig. 10\(b\)](#)) in the heterogeneous porous medium. This indicated  
42 that the capillary and viscous forces affected the pressure fields in heterogeneous  
43 rocks. The results reveal that DPD clearly occurred when the injected fluid (water)  
44 was immiscible with the formation fluid (oil). For SC-CO<sub>2</sub>, the property of miscibility  
45 with hydrocarbon produces a strong seepage effect.  
46  
47  
48  
49  
50  
51  
52  
53  
54  
55  
56

#### 57 **5.5 Well injection with pre-existing fracture**

58  
59 Similar conditions as those in the experiment of Zhang et al. ([Zhang et al., 2017](#))  
60  
61  
62  
63  
64  
65

1 were simulated using the PNM-frac. The formation fluid was assumed to be gas,  
2  
3 which was intended to represent shale gas rock (hydrocarbon wet). The average  
4  
5 pore-throat radius was set to 0.01  $\mu\text{m}$ . The simulation results of pressure distributions  
6  
7  
8 for water and SC-CO<sub>2</sub> injections are presented in Fig. 11. The simulation results  
9  
10 revealed that the DPD derived from the capillary force between water and gas blocked  
11  
12 the spread of pressure (see Fig. 11(a)). However, in the case of SC-CO<sub>2</sub> injection,  
13  
14 pressure spread easily without blocks because of the absence of capillary forces, as  
15  
16 shown in Fig. 11(b). This indicated that the capillary force could cut off the pressure  
17  
18 when the injection pressure was insufficient to overcome the threshold of the capillary  
19  
20 force. It should be noted that the pore pressure in non-invaded elements in this model  
21  
22 was set to 0 MPa.  
23  
24  
25  
26  
27  
28  
29  
30

## 31 **5.6 Discussion of capillary force effect on the fracture geometry**

32  
33 In general, fracturing with water leads to tensile failure, which in turn generates  
34  
35 fractures, and these fractures extend directly in the direction of the main stress. The  
36  
37 simulation results for water injection suggested that the pressure spread was blocked  
38  
39 by the capillary and viscous forces. However, the effect of capillary force on SC-CO<sub>2</sub>  
40  
41 injection was negligible, and the viscous force for SC-CO<sub>2</sub> injection was lower than  
42  
43 for water injection. The pressure could penetrate into the pore and throat around any  
44  
45 pre-existing fracture. This can cause the pore pressure to increase considerably as  
46  
47 compared with using water as injection fluid. When the pore pressure increased, the  
48  
49 effective stress decreased. If we consider the Mohr-Coulomb failure criterion, shear  
50  
51 failure events occur easily with a small effective stress (i.e., high pore pressure), as  
52  
53  
54  
55  
56  
57  
58  
59  
60  
61  
62  
63  
64  
65

1 shown in Fig.12(a). Therefore, increased pore pressure due to SC-CO<sub>2</sub> injection likely  
2  
3 initiates shear failure cracks. Typically, a crack caused by shear failure is not parallel  
4  
5 to a fracture caused by tensile failure (Labuz and Zang, 2012; Patton, 1966).  
6  
7  
8 Fracturing due to SC-CO<sub>2</sub> injection may lead to more branched and high tortuous  
9  
10 fractures as well as rough fracture surfaces. Thus, the fracture geometry derived from  
11  
12 SC-CO<sub>2</sub> injection should be more complex than water injection because of shear  
13  
14 failure cracks (see Fig. 12(b)). These inferred behaviors are consistent with the  
15  
16 experimental results of Zhang et al., who showed that the fracture geometry of  
17  
18 SC-CO<sub>2</sub> was more complex than water fracturing.  
19  
20  
21  
22  
23  
24

25 In fact, this paper is based on a flow model to study different pressure  
26  
27 performances when injecting water and SC-CO<sub>2</sub>. On this basis, combined with the  
28  
29 Mohr-Coulomb failure criterion, it is concluded that SC-CO<sub>2</sub> fracturing should induce  
30  
31 complex fractures. But this conclusion is not directly obtained through simulation.  
32  
33 Therefore, in the following work, we will develop a solid model and couple it with the  
34  
35 flow model to verify the aforementioned results that the fracture pattern induced by  
36  
37 SC-CO<sub>2</sub> fracturing is complex fracture networks.  
38  
39  
40  
41  
42  
43

## 44 **6. Conclusion**

45  
46 A two-phase steady-state flow model considering the effects of capillary and  
47  
48 viscous forces was developed to investigate differences between aqueous and SC-CO<sub>2</sub>  
49  
50 injections. The results of this study can be summarized as follows.  
51  
52  
53

54  
55 With respect to aqueous fluid injection, the pressure field was influenced by the  
56  
57 capillary force because of immiscibility. The capillary force produced DPDs at the  
58  
59  
60  
61  
62  
63  
64  
65

1 interfacial points. The effects of capillary force on aqueous fluid were significant with  
2  
3 respect to low-permeability reservoirs. However, miscible fluid such as SC-CO<sub>2</sub>  
4  
5 reduced the effect of the capillary force and prevented DPD. Miscibility with  
6  
7 hydrocarbon and the low viscosity of SC-CO<sub>2</sub> led to a strong seepage effect. The  
8  
9 strong seepage effect of SC-CO<sub>2</sub> increased pore pressure in wide areas and induced  
10  
11 shear fractures. This typically leads to the formation of complex fracture networks.  
12  
13  
14  
15

### 16 **Acknowledgement**

17  
18 Thank you for previous researchers who use SC-CO<sub>2</sub> to be fracturing fluid and who  
19  
20 contributed to the development of PNM. Their research laid the foundation for my  
21  
22  
23 research.  
24  
25  
26

### 27 **Author contributions**

28  
29 B. Liu planed and conducted the study. A. Suzuki contributed the design of the study.  
30  
31  
32 T. Ito contributed on the examination of the paper structure. All authors participated in  
33  
34 the discussion and interpretation of results, as well as the writing of the manuscript.  
35  
36  
37  
38

### 39 **Funding**

40  
41 This research did not receive any specific grant from funding agencies in the public,  
42  
43 commercial, or not-for-profit sectors.  
44  
45  
46

### 47 **Nomenclature**

48  
49  $g$  conductance,  $m^3/(\text{Pa}\cdot\text{s})$ ;  
50  
51

52  
53  $L$  length of an element,  $m$ ;  
54  
55

56  
57  $n$  number of corners;  
58

59  
60  $z$  number of elements connecting to element  $i$ ;  
61  
62  
63  
64  
65

1  $\alpha_i$  half corner angle at corner  $i$ ;  
2  
3  $P$  pressure, Pa;  
4  
5  
6  $P_c$  capillary pressure, Pa;  
7  
8  
9  $q$  volumetric flow rate,  $m^3/s$ ;  
10  
11  
12  $r$  the curvature radius of corner interface,  $m$ ;  
13  
14  
15  $R$  inscribed radius of a cross-section,  $m$ ;  
16  
17  $\Delta t$  time-step size,  $s$ ;  
18  
19  
20  $\theta$  contact angle, radian;  
21  
22  
23  $\sigma$  interfacial tension between two fluid phases,  $N/m$ ;  
24  
25  
26  $\mu$  fluid viscosity,  $Pa \cdot s$ ;  
27  
28  $V$  fluid volume in an element,  $m^3$ ;  
29  
30  
31  $nw$  non-wetting phase;  
32  
33  
34  $w$  wetting phase;  
35  
36  
37  $C$  conductance of fluid in cross section,  $Pa \cdot s/m^4$   
38  
39  $S_H, S_h$  Maximum principal stress and minimum principal stress  
40

## 41 **Reference**

- 42  
43  
44 Aker, E., JØrgen MÅlØy, K., Hansen, A., Batrouni, G.G., 1998. A two-dimensional  
45 network simulator for two-phase flow in porous media. *Transp. Porous Media* 32,  
46 163–186. <https://doi.org/10.1023/A:1006510106194>  
47  
48  
49  
50  
51  
52 Al-Gharbi, M.S., 2004. Dynamic pore-scale modelling of two-phase flow. Imperial  
53 College London.  
54  
55  
56  
57  
58 Al-Gharbi, M.S., Blunt, M.J., 2005. Dynamic network modeling of two-phase  
59  
60  
61  
62  
63  
64  
65

1 drainage in porous media. *Phys. Rev. E - Stat. Nonlinear, Soft Matter Phys.* 71,  
2  
3 1–16. <https://doi.org/10.1103/PhysRevE.71.016308>  
4  
5

6 Bakke, S., Øren, P.-E., 1997. 3-D Pore-scale modelling of sandstones and flow  
7  
8 simulations in the pore networks. *SPE J.* <https://doi.org/10.2118/35479-PA>  
9

10 Belytschko, T., Organ, D., Gerlach, C., 2000. Element-free galerkin methods for  
11  
12 dynamic fracture in concrete. *Comput. Methods Appl. Mech. Eng.* 187, 385–399.  
13  
14  
15 [https://doi.org/10.1016/S0045-7825\(00\)80002-X](https://doi.org/10.1016/S0045-7825(00)80002-X)  
16  
17

18  
19  
20 Bennour, Z., Ishida, T., Nagaya, Y., Chen, Y., Nara, Y., Chen, Q., Sekine, K., Nagano,  
21  
22 Y., 2015. Crack extension in hydraulic fracturing of shale cores using viscous oil,  
23  
24 water, and liquid carbon dioxide. *Rock Mech. Rock Eng.* 48, 1463–1473.  
25  
26  
27 <https://doi.org/10.1007/s00603-015-0774-2>  
28  
29

30  
31 Blunt, M.J., 2001. Flow in porous media - pore-network models and multiphase flow.  
32  
33  
34 *Curr. Opin. Colloid Interface Sci.*  
35  
36  
37 [https://doi.org/10.1016/S1359-0294\(01\)00084-X](https://doi.org/10.1016/S1359-0294(01)00084-X)  
38

39 Buckley, S.E., Leverett, M.C., 1942. Mechanism of fluid displacement in sands. *Trans.*  
40  
41  
42 *AIME.* <https://doi.org/10.2118/942107-G>  
43

44 Choo, L.Q., Zhao, Z., Chen, H., Tian, Q., 2016. Hydraulic fracturing modeling using  
45  
46 the discontinuous deformation analysis (DDA) method. *Comput. Geotech.* 76,  
47  
48 12–22. <https://doi.org/10.1016/j.compgeo.2016.02.011>  
49  
50

51  
52  
53 Economides, M.J., Boney, C., 2000. Reservoir stimulation. *Reserv. Stimul.*  
54  
55  
56 <https://doi.org/10.1017/CBO9781107415324.004>  
57

58 Higdon, J.J.L., 2013. Multiphase flow in porous media. *J. Fluid Mech.*  
59  
60  
61  
62  
63  
64  
65

1 <https://doi.org/10.1017/jfm.2013.296>

2  
3 Hughes, R.G., Blunt, M.J., 2000. Pore scale modeling of rate effects in imbibition.

4  
5  
6 Transp. Porous Media 40, 295–322. <https://doi.org/10.1023/A:1006629019153>

7  
8  
9 Idowu, N.A., Blunt, M.J., 2010. Pore-scale modelling of rate effects in waterflooding.

10  
11 Transp. Porous Media 83, 151–169. <https://doi.org/10.1007/s11242-009-9468-0>

12  
13  
14 Ishida, T., Chen, Y., Bennour, Z., Yamashita, H., Inui, S., Nagaya, Y., Naoi, M., Chen,

15  
16 Q., Nakayama, Y., Nagano, Y., 2016a. Features of CO<sub>2</sub> fracturing deduced from

17  
18 acoustic emission and microscopy in laboratory experiments. J. Geophys. Res.

19  
20  
21 Solid Earth 121, 8080–8098. <https://doi.org/10.1002/2016JB013365>

22  
23  
24  
25 Ishida, T., Chen, Y., Bennour, Z., Yamashita, H., Inui, S., Nagaya, Y., Naoi, M., Chen,

26  
27 Q., Nakayama, Y., Nagano, Y., 2016b. Features of CO<sub>2</sub> fracturing deduced from

28  
29 acoustic emission and microscopy in laboratory experiments. J. Geophys. Res.

30  
31  
32 Solid Earth. <https://doi.org/10.1002/2016JB013365>

33  
34  
35  
36 Joekar-Niasar, V., Hassanizadeh, S.M., 2012. Analysis of fundamentals of two-phase

37  
38 flow in porous media using dynamic pore-network models: A review. Crit. Rev.

39  
40  
41 Environ. Sci. Technol. 42, 1895–1976.

42  
43  
44  
45 <https://doi.org/10.1080/10643389.2011.574101>

46  
47  
48 Kantzas, Apostolos; Bryan Jonathan; Taheri, S., 2015. Fundamentals of fluid flow in

49  
50 porous media 336.

51  
52  
53 Labuz, J.F., Zang, A., 2012. Mohr-Coulomb failure criterion. Rock Mech. Rock Eng.

54  
55  
56 <https://doi.org/10.1007/s00603-012-0281-7>

57  
58  
59 Latham, J., Guo, L., Wang, X., Xiang, J., 2011. Modelling the evolution of fractures

60  
61  
62  
63  
64  
65



1 using a combined FEM-DEM numerical method. *Harmon. Rock Eng. Environ.*

2  
3 449–454. <https://doi.org/10.1201/b11646-77>

4  
5  
6 Lecampion, B., Bungler, A., Zhang, X., 2017. Numerical methods for hydraulic

7  
8 fracture propagation: A review of recent trends. *J. Nat. Gas Sci. Eng.*

9  
10 <https://doi.org/10.1016/j.jngse.2017.10.012>

11  
12  
13  
14 Liu, Q., Sun, L., Liu, P., Chen, L., 2018. Modeling simultaneous multiple fracturing

15  
16 using the combined finite-discrete element method. *Geofluids* 2018.

17  
18 <https://doi.org/10.1155/2018/4252904>

19  
20  
21  
22 Lu, S., Li, J., Zhang, P., Xue, H., Wang, G., Zhang, J., Liu, H., Li, Z., 2018.

23  
24 Classification of microscopic pore-throats and the grading evaluation on shale oil

25  
26 reservoirs. *Pet. Explor. Dev.* 45, 452–460.

27  
28 [https://doi.org/10.1016/S1876-3804\(18\)30050-8](https://doi.org/10.1016/S1876-3804(18)30050-8)

29  
30  
31  
32  
33 Middleton, R., Viswanathan, H., Currier, R., Gupta, R., 2014. CO<sub>2</sub> as a fracturing

34  
35 fluid: Potential for commercial-scale shale gas production and CO<sub>2</sub> sequestration.

36  
37 *Energy Procedia* 63, 7780–7784. <https://doi.org/10.1016/j.egypro.2014.11.812>

38  
39  
40  
41  
42 Mogensen, K., Stenby, E.H., 1998. A dynamic two-phase pore-scale model of

43  
44 imbibition. *Transp. Porous Media* 32, 299–327.

45  
46 <https://doi.org/10.1023/a:1006578721129>

47  
48  
49  
50 Nguyen, V.H., Sheppard, A.P., Knackstedt, M.A., Val Pinczewski, W., 2006. The

51  
52 effect of displacement rate on imbibition relative permeability and residual

53  
54 saturation. *J. Pet. Sci. Eng.* 52, 54–70.

55  
56 <https://doi.org/10.1016/j.petrol.2006.03.020>

57  
58  
59  
60  
61  
62  
63  
64  
65

- 1 Øren, P.E., Bakke, S., 2003. Reconstruction of Berea sandstone and pore-scale  
2  
3 modelling of wettability effects. *J. Pet. Sci. Eng.*  
4  
5  
6 [https://doi.org/10.1016/S0920-4105\(03\)00062-7](https://doi.org/10.1016/S0920-4105(03)00062-7)  
7  
8
- 9 Øren, P.E., Bakke, S., 2002. Process based reconstruction of sandstones and  
10  
11 prediction of transport properties. *Transp. Porous Media.*  
12  
13  
14 <https://doi.org/10.1023/A:1015031122338>  
15  
16
- 17 Patton, F.D., 1966. Multiple modes of shear failure in rock. 1st Int. Congr. Rock  
18  
19 Mech.  
20  
21
- 22 Peng, P., Ju, Y., Wang, Y., Wang, S., Gao, F., 2017. Numerical analysis of the effect  
23  
24 of natural microcracks on the supercritical CO<sub>2</sub> fracturing crack network of shale rock  
25  
26 based on bonded particle models. *Int. J. Numer. Anal. Methods Geomech.*  
27  
28  
29 <https://doi.org/10.1002/nag.2712>  
30  
31
- 32 Piri, M., Blunt, M.J., 2005. Three-dimensional mixed-wet random pore-scale network  
33  
34 modeling of two- And three-phase flow in porous media. I. Model description.  
35  
36  
37 *Phys. Rev. E - Stat. Nonlinear, Soft Matter Phys.* 71, 1–30.  
38  
39  
40 <https://doi.org/10.1103/PhysRevE.71.026301>  
41  
42
- 43 Reynolds, C.A., Blunt, M.J., Krevor, S., 2018. Multiphase Flow Characteristics of  
44  
45 Heterogeneous Rocks From CO<sub>2</sub> Storage Reservoirs in the United Kingdom.  
46  
47  
48 *Water Resour. Res.* <https://doi.org/10.1002/2017WR021651>  
49  
50
- 51 Shi, F., Wang, X.L., Liu, C., Liu, H., Wu, H.A., 2017. An XFEM-based method with  
52  
53 reduction technique for modeling hydraulic fracture propagation in formations  
54  
55  
56 containing frictional natural fractures. *Eng. Fract. Mech.* 173, 64–90.  
57  
58  
59  
60  
61  
62  
63  
64  
65

- 1 Shimizu, H., Murata, S., Ishida, T., 2011. The distinct element analysis for hydraulic  
2  
3 fracturing in hard rock considering fluid viscosity and particle size distribution.  
4  
5  
6 Int. J. Rock Mech. Min. Sci. 48, 712–727.  
7  
8  
9 <https://doi.org/10.1016/j.ijrmms.2011.04.013>  
10
- 11 Valvatne, H., 2004. Predictive pore-scale modelling of multiphase flow 146.  
12
- 13 Vilarrasa, V., Bolster, D., Dentz, M., Olivella, S., Carrera, J., 2010. Effects of CO<sub>2</sub>  
14  
15 compressibility on CO<sub>2</sub> storage in deep saline aquifers. Transp. Porous Media.  
16  
17  
18  
19  
20 <https://doi.org/10.1007/s11242-010-9582-z>  
21
- 22 Wang, S., Feng, Q., Dong, Y., Han, X., Wang, S., 2015. A dynamic pore-scale  
23  
24 network model for two-phase imbibition. J. Nat. Gas Sci. Eng. 26, 118–129.  
25  
26  
27  
28  
29 <https://doi.org/10.1016/j.jngse.2015.06.005>  
30
- 31 Watanabe, N., Egawa, M., Sakaguchi, K., Ishibashi, T., Tsuchiya, N., 2017. Hydraulic  
32  
33 fracturing and permeability enhancement in granite from subcritical/brittle to  
34  
35  
36  
37  
38 supercritical/ductile conditions. Geophys. Res. Lett. 44, 5468–5475.  
39  
40 <https://doi.org/10.1002/2017GL073898>  
41
- 42 Yan, C., Zheng, H., Sun, G., Ge, X., 2016. Combined finite-discrete element method  
43  
44  
45 for simulation of hydraulic fracturing. Rock Mech. Rock Eng. 49, 1389–1410.  
46  
47  
48 <https://doi.org/10.1007/s00603-015-0816-9>  
49
- 50 Zhang, X., Lu, Y., Tang, J., Zhou, Z., Liao, Y., 2017. Experimental study on fracture  
51  
52  
53  
54 initiation and propagation in shale using supercritical carbon dioxide fracturing.  
55  
56  
57 Fuel 190, 370–378. <https://doi.org/10.1016/j.fuel.2016.10.120>  
58
- 59 Zhao, Q., Lisjak, A., Mahabadi, O., Liu, Q., Grasselli, G., 2014. Numerical simulation  
60  
61  
62  
63  
64  
65

1 of hydraulic fracturing and associated microseismicity using finite-discrete  
2  
3 element method. *J. Rock Mech. Geotech. Eng.* 6, 574–581.  
4

5  
6 <https://doi.org/10.1016/j.jrmge.2014.10.003>  
7  
8  
9  
10  
11  
12  
13  
14  
15  
16  
17  
18  
19  
20  
21  
22  
23  
24  
25  
26  
27  
28  
29  
30  
31  
32  
33  
34  
35  
36  
37  
38  
39  
40  
41  
42  
43  
44  
45  
46  
47  
48  
49  
50  
51  
52  
53  
54  
55  
56  
57  
58  
59  
60  
61  
62  
63  
64  
65

## \*Highlights

The seepage effect estimation model for supercritical CO<sub>2</sub> and water fracturing in unconventional gas reservoir is proposed.

The simulation results show that capillary force has strong effect on seepage effect.

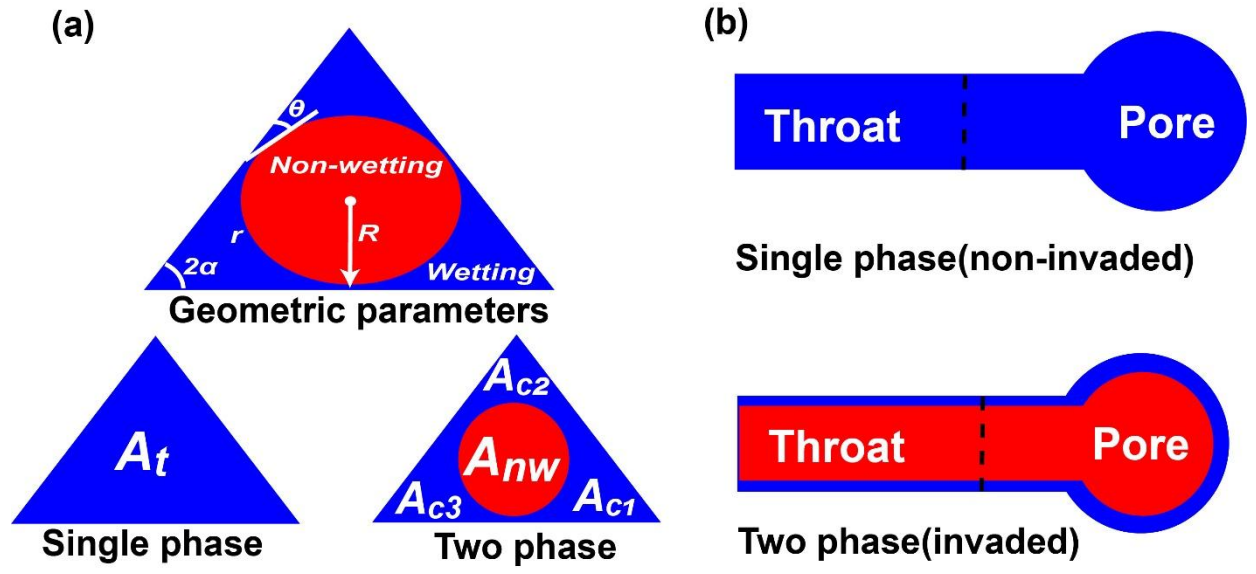
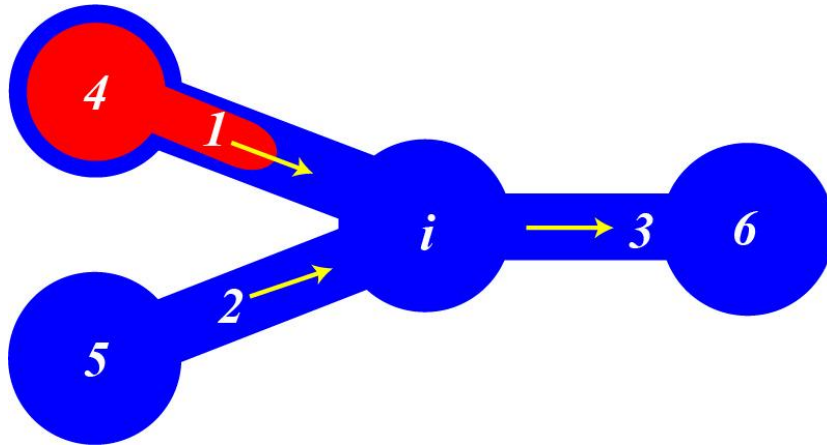
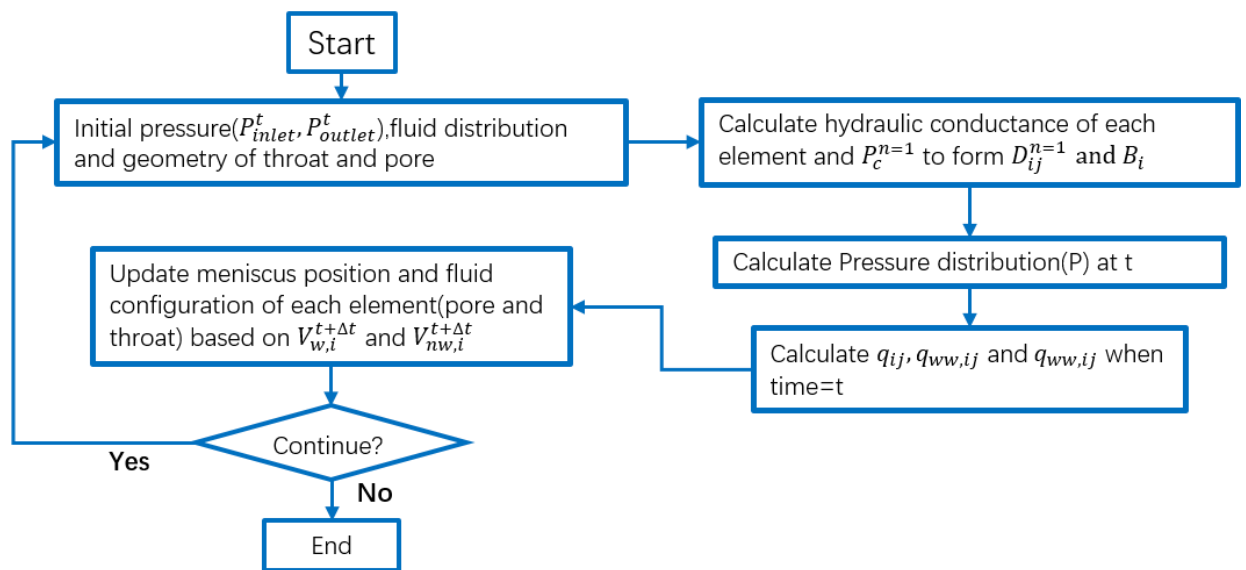


Fig. 1. Schematic image of configuration.



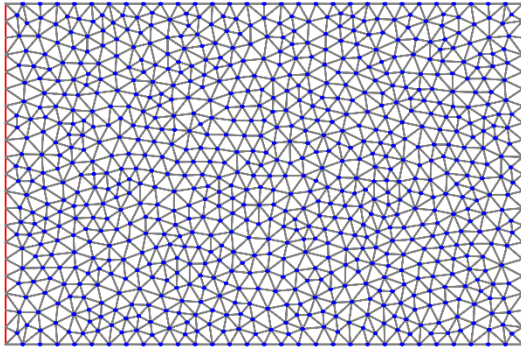
**Fig. 2.** Schematic diagram of volume flux conversation. The yellow arrows represent the flow direction.








**Fig. 3.** Computational procedure.



Network A:



Inlet side:		Pore:	
Outlet side:		Throat:	
Fracture:			

Network B:

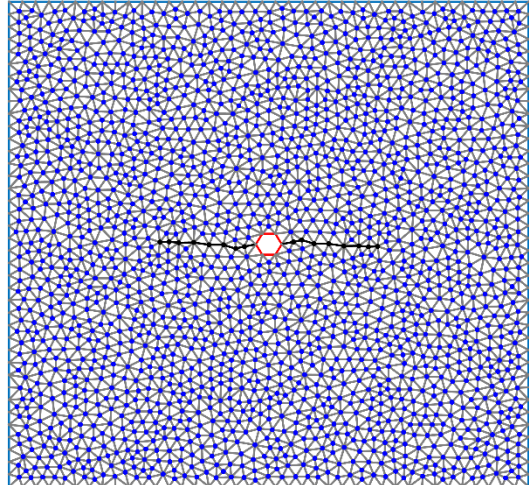


**Fig. 4.** Structure of pore network for simulation.

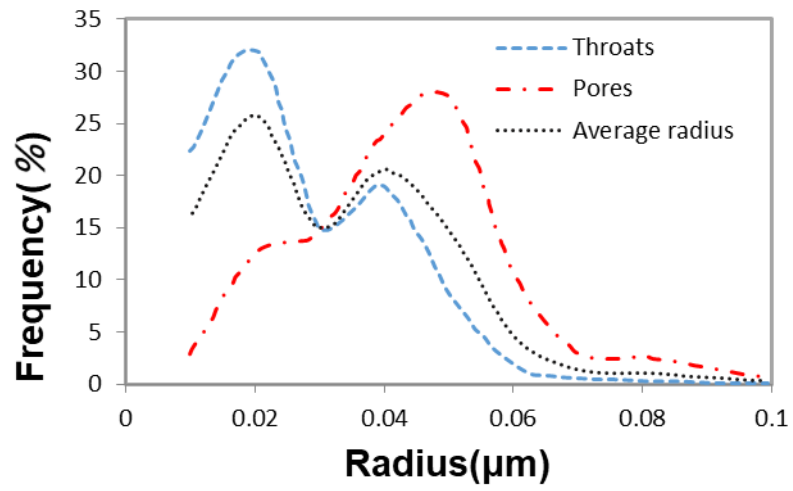


**Fig. 5.** Pore and throat size distributions for heterogeneous porous medium (PNM-hetero).

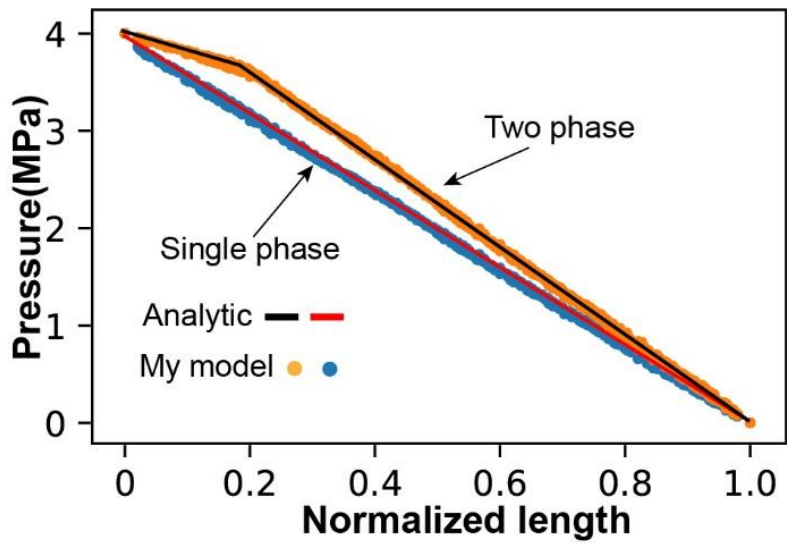


**Fig. 6.** Validation of flow model using PNM-homo.

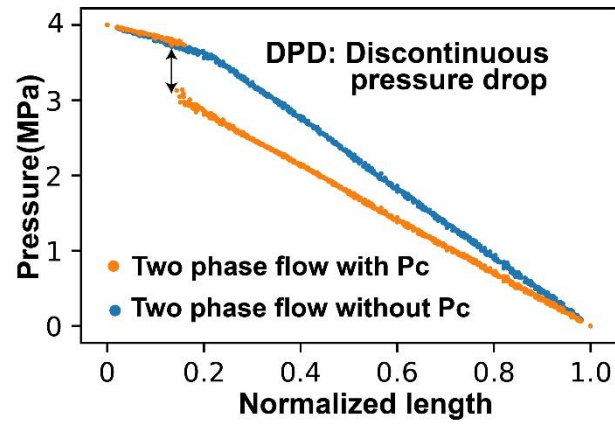


**Fig. 7.** Effect of capillary force on pressure field using PNM-homo.

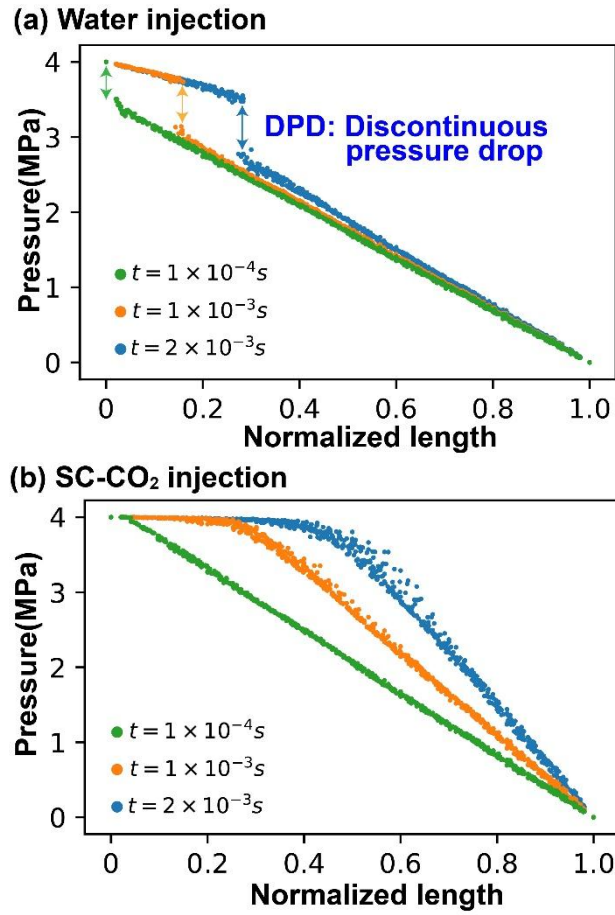
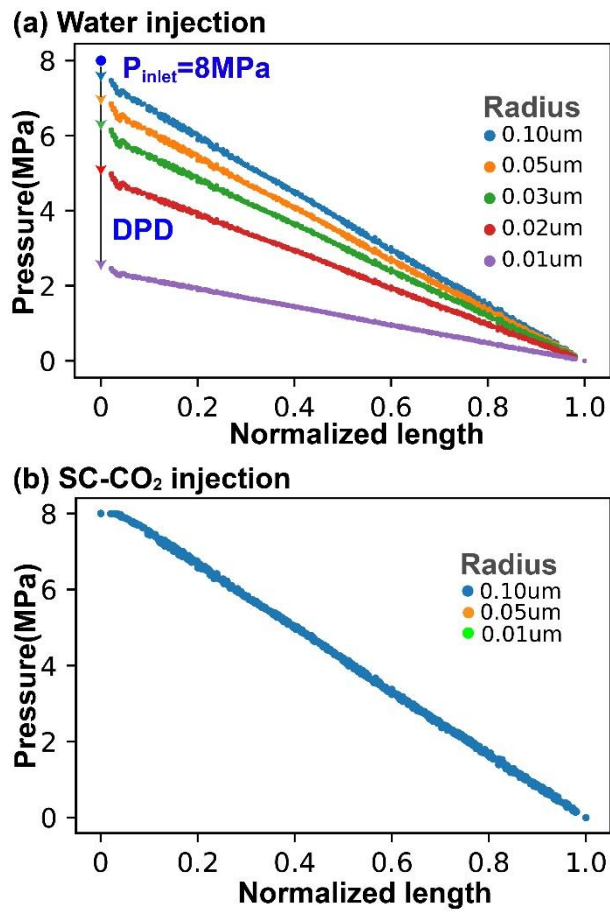
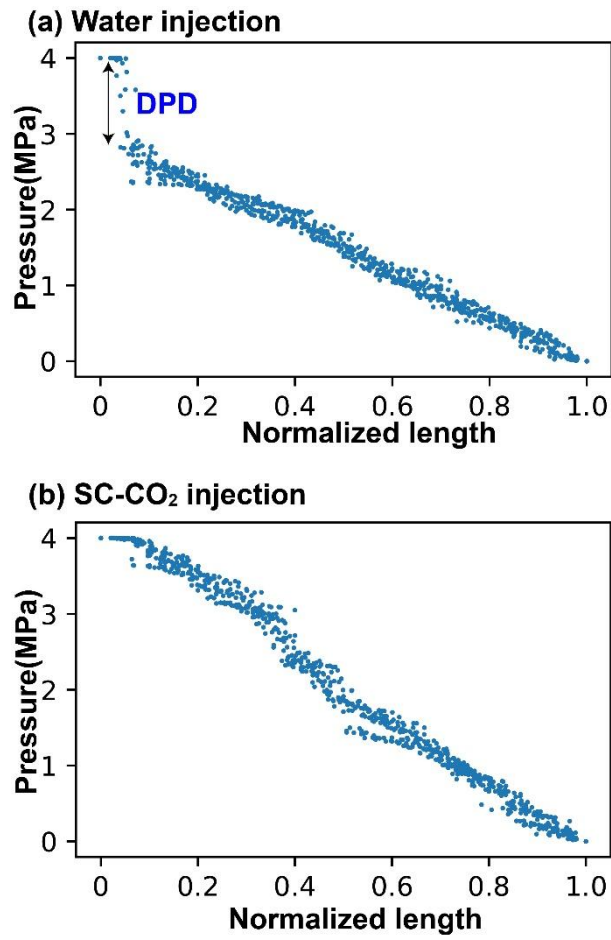


Fig. 8. Pressure field of different injection time using PNM-homo.



**Fig. 9.** Pressure field of different pore-throat radius using PNM-homo.



**Fig. 10.** Pressure field of two-phase flow considering capillary force using PNM-hetero.

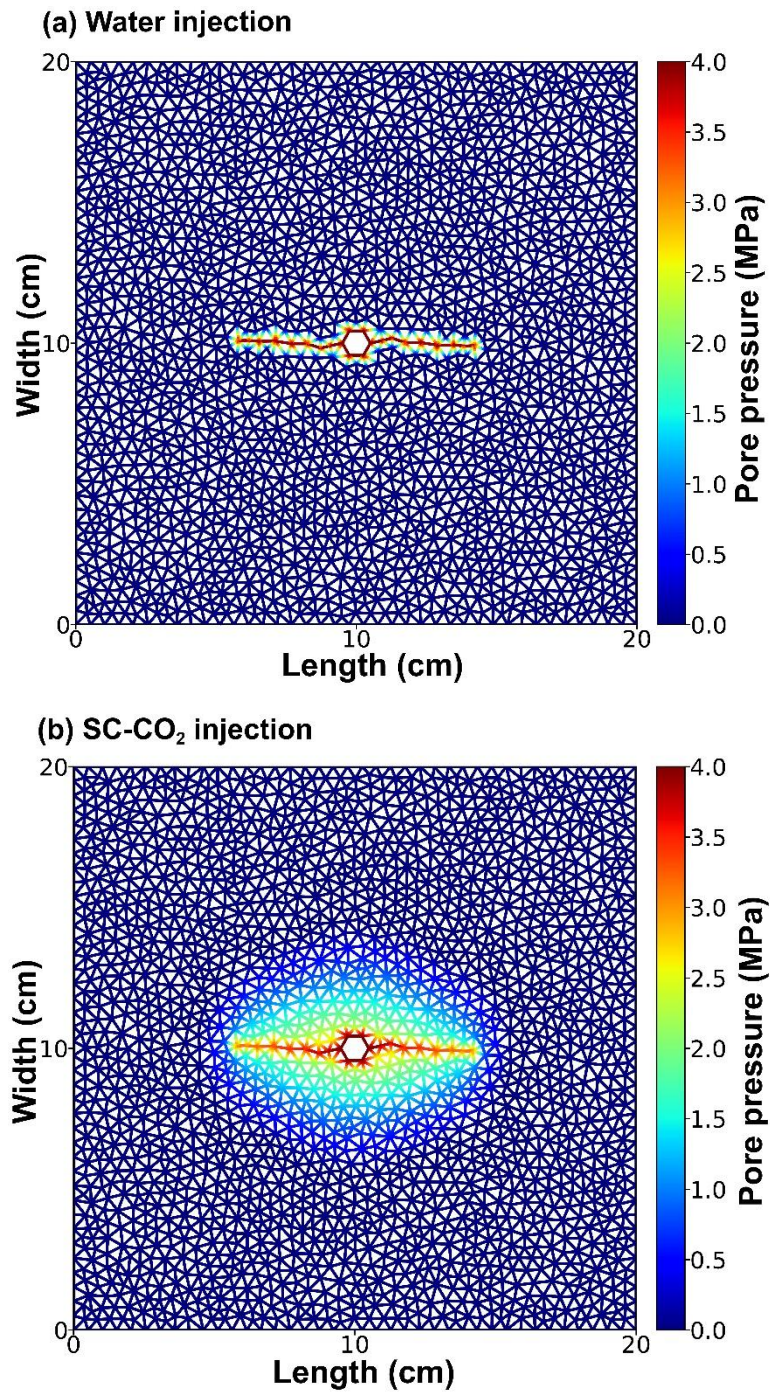
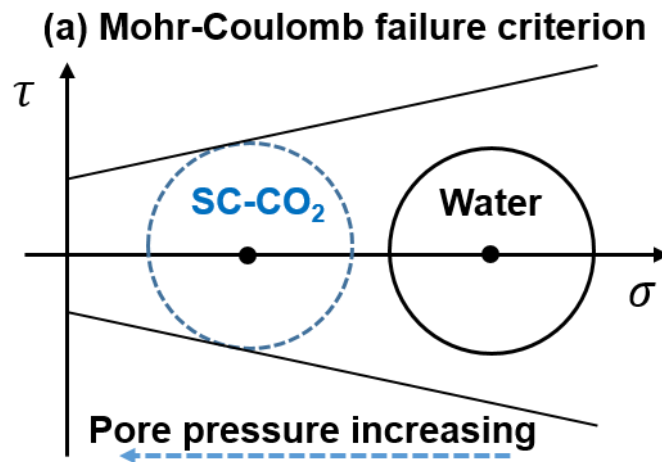


**Fig. 11.** Pressure field due to water injection and SC-CO<sub>2</sub> injection in homogenous porous medium with pre-existed fractures using PNM-frac.





(b) Geometry of fracture

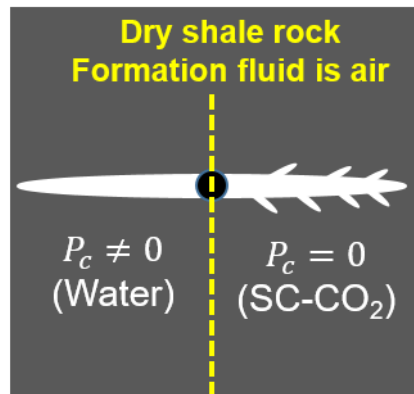


**Fig. 12.** (a) Schematic diagram of Mohr-Coulomb failure criterion and (b) geometry of different type of fractures.

**Table 1** Simulation sample size and average radius of pore-throat.

Simulation sample	Average pore-throat radius ( $\mu m$ )	Size of model ( $mm \times mm$ )
1	0.15	$0.225 \times 0.15$
2	0.10	$0.150 \times 0.10$
3	0.05	$0.075 \times 0.05$
4	0.03	$0.045 \times 0.03$
5	0.02	$0.030 \times 0.02$
6	0.01	$0.015 \times 0.01$

**Table 2** Fluid systems for simulation.

Fluid system (injection - formation)	Contact angle ( $deg$ )	Interfacial tension ( $mN/m$ )
Water-Gas	0	50.0
SC-CO <sub>2</sub> -Gas	Miscible	Miscible
Water - Oil	30	30
SC-CO <sub>2</sub> -Oil	Miscible	Miscible

**Table 3** Fluid viscosity.

Fluid	Viscosity ( $mPa \cdot s$ )
Gas	0.011
Water	0.89
Oil	4.0
SC-CO <sub>2</sub>	0.02

**Table 4** Simulation cases.

Simulation	Injecting fluid	Formation fluid	Inlet pressure (MPa)	Outlet pressure (MPa)	Injection time ( $10^4$ s)	Network
Validation	Oil/Water	Oil	4.0	0	2.0	PNM-homo
5.1	Water	Oil	4.0	0	2.0	PNM-homo
5.2	Water/SC-CO <sub>2</sub>	Oil	4.0	0	1.0-20	PNM-homo
5.3	Water/SC-CO <sub>2</sub>	Oil	8.0	0	2.0	PNM-homo
5.4	Water/SC-CO <sub>2</sub>	Oil	4.0	0	2.0	PNM-hetero
5.5	Water/SC-CO <sub>2</sub>	Gas	4.0	0	1200	PNM-frac

**Table 5** Classification of shale oil reservoirs.

Classification	Permeability ( $10^{-3} \mu m^2$ )	Average pore-throat radius ( $\mu m$ )
I	> 1	> 0.15
II	1~0.4	0.15~0.07
III	0.40~0.05	0.01~0.07
IV	< 0.05	< 0.01